UNIVERSITAT POLITÈCNICA
DE CATALUNYA
BARCELONATECH

Ph.D. thesis:

CONTRIBUTIONS TO THE DETERMINATION OF ELECTROMAGNETIC BIAS IN GNSS-R ALTIMETRY

by Ali Ghavidel

Advisor Professor Adriano Camps

Remote Sensing Laboratory

Department de Teoria del Senyal i Comunicacions

Universitat Politècnica de Catalunya, Barcelona-Tech

Barcelona, Spain

May 2015

Abstract

In this work, ocean altimetry using Global Navigation Satellite Systems Reflectometry is studied. Among the different error sources in GNSS-R altimeters, the electromagnetic bias (EM) bias is analyzed in this Ph.D. Thesis. It has been a matter of research for several decades in conventional nadir-looking radar altimetry, but it is quite new in GNSS-R altimetry.

In this Ph.D. Thesis, previous studies on the EM bias are revised first for both nadir-looking and off-nadir looking scenarios. In general, there are three main methods to compute the EM bias: the Weakly Non-Linear theory (WNL), the Modulation Transfer Function (MTF), and combined models of both. In this Ph.D. Thesis, a brief study on both the WNL and the MTF is performed, the combined model is then selected, simulated, validated at Ku and C-bands, and then extrapolated at L-band. Secondly, the EM bias is studied in the time-domain and characterized using statistical descriptors. Finally, the impact of natural phenomena such as rain swell, and currents on the EM bias is computed numerically.

In conclusion, this Ph.D. Thesis has shown that the EM bias is not only a function of the wind speed, but also it is a function of both the incidence and the azimuthal angles as well. The time-domain study has demonstrated that it has a non-linear behavior. Moreover, heavy rains decrease the EM bias, while swell and currents (with opposite direction to that of the wind speed) increase the EM bias. Nevertheless, while the current has the same direction of wind speed, the EM bias is reduced.

Acknowledgements

This work has supported by the Spanish National Research project AYA2011-29183-C02-01 from the Ministry of Economy and Competitiveness. First, I have to acknowledge Professor Adriano Camps for offering me the opportunity to perform my PhD in his group, and his guidance patiently during several years. Secondly, I acknowledge Drs. Isaac Ramos, and Verónica Gonzalez to provide articles and some experience, and the technicians Mr. Joaquim Giner, Ruben Tardío, Albert Martón, for all their help to assist me. I would like to say thank to Mrs. Beni Vazquez, Aynie Khoe and Teresa Pons for taking care of all the administrative stuff, dealing with the paperwork. This PhD Thesis is also in debt with all my team colleagues from the beginning Alberto Alonso, Daniel Pascual, Jorge Querol, Francisco Martín, and Raúl Onrubia. All of them made the work easier for me. Finally, I must thank special to my spouse (Nasibeh) for letting being alone, and to my parents who supported me during my Ph.D.

Table of Contents

List of Figures

List of Tables

List of Acronyms

ADC Analog-to-Digital Converter

BPF Band-Pass Filter

C/A Coarse Code

cGNSS-R Conventional GNSS-R

CYGNSS Cyclone Global Navigation Satellite Systems

DDM Delay-Doppler Map

DLL Delay Locked loop

DORIS Doppler Orbitography and Radio-position Integrated by Satellite

DSD rain Drop Size Distribution

EM Electromagnetic Bias

ESA European Space Agency

GDOP Geometric Dilution Of Precision

GLONASS GLObal NAvigation Satellite System

GNSS Global Navigation Satellite System

GNSS-R GNSS Reflectometry

GO Geometric Optics

GPS Global Positioning System

GTD Geometrical Theory of Diffraction

HOW Hand Over Word

IBC Impedance Boundary Condition

IF Intermediate Frequency

iGNSSR Interferometric GNSS-R

IRNSS Indian Regional Navigation Satellite System

JONSWAP Joint North Sea Wave Observation

KA Kirchhoff Approximation

LEO Low Earth Orbit

LHCP Left Hand Circular Polarization

LNA Low Noise Amplifier

LRA Laser Reflectometry Array

MOM Method Of Moment

MSL Mean Sea Level

MT Modal Technique

P Precise code

PARIS-(IoD) Passive Reflectometry and Interferometry System, In-Orbit Demonstrator

PDF Probability Density Function

PLL Phase Locked loop

PO Physical Optics

PRN Pseudo-Random Noise

PTD Physical Theory of Diffraction

PVT Position, Velocity, and Time

QZSS Quasi-Zenith Satellite System

MEO Medium Earth Orbit

MTF Modulation Transfer Function

RCS Radar Cross-Section

RF Radio Frequency

RHCP Right Hand Circular Polarization

SNR Signal-to-Noise Ratio

WKB Wentzel Kramers Brillouin

SWADE Surface Wave Dynamic Experiment

SWH Significant Wave Height

TDS Tech-Demo-Sat

THC ThermoHaline Circulation

TLM Telemetry

UTC Universal Time Coordinate

WAF Woodward Ambiguity Function

WNL Weakly Non-Linear

Chapter 1 - Introduction

One of the most promising methods proposed to maximize the altimetry data coverage is to receive the reflected signals transmitted by satellites of the Global Navigation Satellite Systems (GNSS), and particularly the Global Positioning System (GPS) [1]. Usually, a GPS receiver in a Low Earth Orbit (LEO) can track up to 10 GPS reflections at the same time. GNSS-R altimeters would be placed in LEO and can use direct GNSS signals and the reflected ones from the ocean surface to study sea surface properties such as, height, surface roughness, wind speed, etc. For example, by computing the delay between the direct and the reflected signals, the sea surface height can be obtained. The received signal magnitude depends on some parameters such as, the incidence angle, the sea surface roughness, etc. The main drawback of this method is the poor accuracy, related to the small bandwidth, and the poor Signal to Noise Ratio (SNR), which affects the delay estimation. Delays have different components: geometric delay, ionospheric delay, instrument delay, and delays introduced by the way the signals scatter on the surface etc. There are different methods to compensate for each type of the above cited delays. However, the estimation of the so-called electromagnetic bias (EM bias) at L-band, and in a bistatic configuration, remains a matter of research, and it is the object of the study of this Ph.D. Thesis.

Mesoscale ocean altimetry was applied by nadir-looking radar altimeters. The first spaceborne altimeters are found on board of the Skylab, GEOS-3, and Seasat in the 1970's [2]. In order to monitor the mesoscale variability at high special and temporal resolution at least two altimeter missions are required. With a single altimeter mission is not possible to resolve the main space and time scales of the ocean.

Nowadays, satellite altimeters are one of the most successful in all Earth science missions. The ocean surface is studied by the majority of altimetry applications, because of the impacts of the ocean movements on climate, and vice-versa. Satellite altimeters basically determine the distance from the satellite to a target surface by measuring the satellite-to-surface round-trip time of the transmitted radar pulse. Their main limitation is the nadir-looking configuration.

The magnitude and shape of the echoes (or "waveforms") also contain information about the characteristics of the surface which caused the reflection. Several different frequencies can be used for radar altimeters. The choice depends on the mission objectives and constraints, the technical possibilities etc. Each frequency band has its advantages and disadvantages. It means for higher frequency bands, more transmitted power is required (e.g. Ku-band), as free space losses are larger and much more it surfers from atmospheric attenuation, but it has been demonstrated that has less EM bias as compared to C-band. At L-band, attenuation is even smaller and does not need a dedicated transmitter, but the EM bias is expected to be higher as well. At L-band, dedicated transmitters are not required because of the presence of GNSS signals opportunity. Another important phenomena is the Faraday rotation effect (interaction between the Earth's magnetic field and electromagnetic wave), which is investigated using circular polarization waves [3], [4].

When the wind blows over the ocean water, it changes the ocean's surface, first into undulating and then into waves. Once the surface becomes rough, the wind has a constantly increasing, so the sea surface will become roughness entirely.

Actually, in altimetry systems, the round-trip time of pulse is used to calculate the height distance (from satellite to the ocean surface). As it is known, the sea surface with roughness has crests and troughs, that both will reflect the

electromagnetic waves, but with a discrepancy. These different scattered waves (more from the troughs and less from the crests) from the same area will introduce the error in the estimated height of altimetry systems.

The EM bias degrades the accuracy of altimetry observations and must be quantified. Several theoretical and experimental works have been performed to estimate the EM bias [5]–[10]. Generally these works can be divided into two categories depending on the incidence angle: nadir and off-nadir incidence angle. A few methods to estimate the off-nadir EM bias have been recently reported by [11]–[14], with aircraft mounted radar instruments.

The sea surface height varies from the scale of centimetres to meters due to wind-driven waves. Depending on the roughness and observation conditions, some scattered waves arrive a bit early, due to the wave crests, and some arrive a bit late, which spreads the radar returns over time. The estimated time of arrival indicates the mean surface height over the illuminated area. In simple terms, the EM bias occurs because the reflection of the radar signal from wave troughs is lesser than from the crests. Satellite-based work by [13] has shown that the bias exists, that it has a frequency dependence, and that it is related to the sea state.

1.1- State of the Art and Historical Revision

GNSS-R can receive both off-nadir and nadir reflected signals, but in principle off-nadir reflected signals are less reliable for geophysical data interpretation. On the other hand, a conventional GNSS-R receiver can collect both the direct and the reflected signals, and then produces the waveform (cross-correlation between the received signal and its locally generated replica) of the reflected GPS signals (and eventually the direct signals, as

well). The shape of reflected waveform is very different as compared to the direct waveform, in shape, time delay, and signal amplitude. The time delay has a significant effect on the data interpretation, and should be studied more precisely. By taking the derivative of the waveform, the delay at the specular reflection point can be extracted [15].

One of the most challenging error sources to correct for in satellite altimetry is the so called EM bias that affects the precision of the altimetry measurements. The EM bias is originated by the anisotropy of the wave shape where the scattering is actually taking place (i.e. the valleys of the waves are flat, while the crests are peaky). Nowadays, the evaluation of EM bias in a bistatic, forward-scattering configuration at L-band such as in GNSS-R is still a matter of research and it is the object of this Ph.D. thesis. In addition, the EM bias is considered in this Ph.D. Thesis in the time-domain and characterized statistically. In addition, the presence of rain, swell, and surface current have studied.

The EM bias problem was reported, when the TOPEX/POSEIDON satellite-borne radar altimeter encountered problems in a series of 11 aircraft flights during the Surface Wave Dynamics Experiment (SWADE) in [12].

At nadir (incidence angle=0^o), many experimental and theoretical studies have been performed [5]–[8], [10], [13], [16], [17]. However, few off-nadir incident angle, experimental and theoretical studies have been reported [11]–[13].

In this work, the EM estimation models, the Weakly Nonlinear (WNL), and the Modulation of Transfer Function (MTF) are revised, and combined. This bias model depends on the separation wave-number between the long and the short waves (cut-off wave-number). Theoretical predictions and experimental

results of this work have confirmed that the EM bias has an angular dependency, and by increasing the incidence angle, bias sign can even change its sign. In [13], a relationship between the radar cross-section and the incidence angles was derived for backscattering of using the Physical Optics (PO) scattering model. It is known, that the radar cross-section has a strong influence on the EM bias magnitude, but in this work that relationship is derived for the Geometrical Optics (GO) scattering (instead of short-wave effects on the EM bias). In addition, the Physical Optics scattering method is applied to compute EM bias more precisely. Finally, the EM bias magnitude for different incidence angles is estimated.

The second objective of this Ph.D. Thesis is to study up to which surface roughness conditions the tracking of the coherent reflected GNSS signal by a standard GNSS receiver is possible. For this purpose, the acquisition module of a GPS software receiver has been implemented to simulate its behaviour for the reflected GPS signals over the sea surface.

Third, the EM bias is considered in the time-domain using a numerical method and described by statistical descriptors, which are not considered yet. In fact, the time-domain EM bias provides an opportunity to investigate its behavior.

Finally, some natural phenomena (rain, swell, and current) are added to the ocean surface and then, their impact on EM bias is considered using the numerical method, which was also not considered in previous EM bias reports. In this part, these phenomena surface spectra (including rain, swell, and currents) have used to investigate their impacts on the EM bias.

1.2- Altimetry

Remote sensing using free-source signals opened a new era to the Earth observation, in relevant applications such as: meteorology, climate monitoring, marine science, etc. New generations of LEO satellites are using the GNSS signals for radio-occultations, and wind retrieval, and for altimetry systems. Using GNSS signals has several advantages, they are all-weather, real time, and continuously available. Here, an introduction to the conventional altimetry, GNSS-R altimetry (particularly the Passive Reflectometry and Interferometry System (PARIS)), and the GNSS systems are presented.

1.2.1- Conventional Altimetry

Basically, satellite altimetry indicates the distance between the satellite and the target surface by measuring the satellite-to-surface round-trip time of a radar pulse. Actually, radar altimetry was used to measure the height. In addition, a lot of other information can be extracted from altimetry system. The altimeter transmits a radar wave and analyses the returned wave that bounces off the surface. The magnitude and shape of scattered wave (waveform) contains information about the surface characteristics, which caused the reflection. Over the ocean surface, the scattered wave has a characteristic shape that can be described analytically, as originally proposed in [18].

Plenty of information can be extracted from the reflected waves, such as:

1- The amplitude of scattered wave can be used to compute σ^o.
2- The time-delay can be used to estimate the average sea surface height.

3- The skewness shows the leading edge of waveform.
4- The Trailing edge of slope is linked to the deviation of the radar from the nadir point.
5- The waveform is linked to the thermal noise.

To obtain accurate measurements within a few centimeters from a range of several hundred kilometers, a precise knowledge of the satellite's orbital position is required. Thus, several positioning systems are usually carried onboard altimetry satellites.

Radar altimeters of the satellite transmit waves at high frequencies towards the Earth's surface, and receive the echo from the surface (the "waveform"). The waveform will be processed to derive a precise measurement of the time taken to make the round trip between the satellite and the surface. This time measurement, scaled by the speed of light, produces a range measurement.

Topex/Poseidon was launched in 1992, and it was designed at Ku-band to make inter-comparisons with previous instruments. It was used to observe the surface circulation of the oceans, tides, and currents (see Figure 1.1). This satellite was equipped with three instruments in order to derive its location accurately.

The first one was the NASA Laser Reflectometry Array (LRA). The Doppler Orbitography and Radio-positioning Integrated by satellite tracking receiver (DORIS) consisted of an on-board receiver and a global network of ground-based transmitters. The third system was an on-board GPS receiver to determine the satellite position continuously.

Figure 1.1 TOPEX/Poseidon launched in 1992[20].

1.2.2- GNSS-R Altimetry

A new generation of low-orbit satellites is trying to design possible lightweight, for example, by removing the transmitter. TOPEX/Poseidon was the first mission to validate that the GPS System have used to determine a spacecraft's exact position and track it in orbit constantly. Knowing the satellite's precise position to within 2 centimeters (or less than 1 inch) in altitude provided the great opportunity for accurate ocean height measurements possible.

Satellite altimeters measure the distance from the satellite to the sea surface by measuring the round-trip time of a radar pulse, typically in a nadir-looking configuration. The amplitude and shape of the so-called waveform (cross-

correlation of the signal received by a down-looking antenna and the locally-generated replica of the transmitted signal) include information of the characteristics of the surface where the scattering takes place. Conventional radar altimeters use a nadir-looking configuration, high transmitted power, large bandwidth, and high carrier frequency to be less sensitive to ionospheric effects. On the other hand, upcoming GNSS-R altimeters use a bistatic (off-nadir) configuration, much lower transmitted power, narrower bandwidth[1], and use frequency bands allocated for radio-navigation[2].

As compared to the conventional altimeter radar, these limitations translate into a poorer height resolution, although the spatial-temporal sampling is maximized by receiving reflected navigation signals from a wide range of incidence angles [1].

Fortunately, there is plenty of GNSS signals available continuously. For example the GLObal NAvigation Satellite System (GLONASS) contains at least 24 MEO satellites in three orbital planes recently launched recently by the Russian Federation [19]. Moreover there are other GNSS systems under development such as: Galileo (European Union), Beidou (China), Quasi-Zenith Satellite System (QZSS-Japan), and India's Regional Navigation Satellite System (IRNSS) [20]–[23].

---

[1]In conventional GNSS-R (cGNSS-R) the bandwidth is limited to the bandwidth of the publicly available codes (e.g. ~2 MHz for the GPS L1 C/A code). In interferometric GNSS-R (iGNSS-R) the bandwidth is limited to the bandwidth of the whole navigation signals (e.g. ~25 MHz for the GPS composite signal resulting from the combination of the C/A, P and M codes). C/A stands for Coarse/Acquisition, P for Precise, and M for Military pseudo-random noise (PRN) codes.

[2]Typically L1 (1575.420 MHz) and L2 (1227.600 MHz), or L1 and L5 (1176.450 MHz), in order to compensate for ionospheric effects.

In a GNSS-R instrument, the observing information is obtained by the complex cross-correlation of the scattered signals either with a locally generated replica of the transmitted signal (conventional GNSS-R or cGNSS-R), or with the direct down-looking signal (interferometric GNSS-R or iGNSS-R) during the coherent integration (by an incoherent integration to reduce speckle noise).

Mesoscale ocean altimetry was a challenging issue for satellite observations. In order to solve it, the Passive Reflectometry and Interferometry System (PARIS) have been proposed using GNSS reflected signals that applied as a tool to perform ocean altimetry along several paths simultaneously from a wide swath (1000 km). PARIS is able to provide mesoscale ocean altimeter with ~30 cm accuracy using GNSS signal. PARIS altimeter instrument has actually used the interferometry concept to measure the distance. It includes: an up-looking antenna, a down-looking antenna, and down-conversion steps and signal processing. The up-looking antenna receives signals emitted by one or more satellites emitters (GNSS) directly. The down-looking antenna is directed to the Earth and receives replicas of these same signals reflected by the ocean surface.

GNSS-R instruments can compute the electromagnetic delay between the transmitter and the receiver, after the signal scattered from the sea surface. The delay is the combination of several types of delays: a geometric component delay, atmospheric delays (ionospheric and tropospheric effects), and instrumental delays (clock errors, sub-system delays, and antenna offsets), and noise. Delays are usually called range (in the space domain) or delay indistinctly, after multiplying by the speed of light. In altimetry, indicating the vertical height is simple corresponds to an average or statistical central tendency of the instantaneous surface height across the footprint. It requires

being distinguished from the Mean Sea Level (MSL) at that same location, which is the measure of the average height after a long time series.

The time delay of the scattered wave can be estimated from the delay of the maximum derivative of the waveform [24]. Actually, there are different contributions to the estimated delay: the geometric delay, the offset between the receiver and transmitter clocks, and the ionospheric delay. Generally, a down-looking antenna collects the reflected GNSS signal and it is cross-correlated with a locally generated replica of the transmitted open codes. In order to reduce error, the direct zenith signal can be collected as a reference of either the signal's power and/or delay. The mentioned delay has the most significant role on the altimetry precision that is shown in relationship [25]:

$$\sigma_h = \frac{\upsilon}{2.\sin\theta_e}.\sigma_\tau(B), \tag{1.1}$$

where υ is the average speed of light, and θ_e is elevation the angle, B and σ_τ are the instrument's bandwidth and the optimum achievable delay precision. Comprehensively, this parameter (σ_τ) has been investigated in [25] in order to optimize the generic GNSS-R performance. The EM bias is one the main error in this time delay, which has a direct relation of altimetry height accuracy.
The conventional PARIS configuration performs the cross-correlation with on-board generated replica of open access codes. This configuration would experience a degradation of the SNR at the correlation output due to the additional thermal noise in the received direct signal. An increase in SNR using swap of integration times has been recently proposed in order to optimize iGNSS-R performance [25].

As the altimetry precision depends on the delay precision and delay precision is related to the SNR [26]:

$$\sigma_\tau \geq \frac{1}{\sqrt{SNR(B)}} \cdot \frac{1}{2\pi\beta(B)}, \quad (1.2)$$

The SNR of received signal of the PARIS-IoD instrument is expressed in [27]:

$$SNR = \frac{SNR_{cr}}{1 + \frac{1 + SNR_R}{SNR_D}}, \quad (1.3)$$

where B is the instrument bandwidth, and β is the Gabor bandwidth, and SNR_{cr}, SNR_D, and SNR_R are SNRs of without the thermal noise (clean replica), SNR of the direct signal, and SNR of the reflected respectively. Moreover, the SNR is proportional to the coherent integration time that is expressed in [27]:

$$SNR \propto T_{coh} \cdot \sqrt{N_i}, \quad (1.4)$$

where $N_i$is the total number of incoherent average signals. On the other side, the T_{coh} is limited by coherence time of observed surface, which is estimated using [28]:

$$\tau_s = \frac{\lambda}{2.v} \sqrt{\frac{h}{2.c.\tau_c.\cos(\theta_i)}}, \quad (1.5)$$

where h, λ, and v are the receiver height, GNSS signal wavelength, and receiver velocity respectively, and also c, τ_c, and θ_i are the light speed, the chip duration (1μs) and observation angle as well.

In addition to the geometric delay, there are several other contributions to the estimated average delay: the offset between the receiver and transmitter clocks, and the tropospheric, and the ionospheric delays. The tropospheric dry delay has an average value of 2.3 m, and a residual error of ~0.7 cm, and the tropospheric wet delay is highly variable, typically from 5 to 30 cm, and it is computed using atmospheric models or microwave radiometers, with a precision of ~1.1 cm. The ionospheric delay is also highly variable, typically

from 1 to 20 cm, and it is computed using dual-frequency observations with a precision of ~ 0.5 cm.

In [25] details of the altimetry error budget for an iGNSS-R instrument was performed to assess the rms altimetry precision. The main results are summarized in Table 1.

Table 1.1 Instrument performance for a PARIS IoD – like instrument at levels 1 (range precision) and 2 (height precision) including ionospheric corrections for GPS and Galileo at $\theta_i = 0^{\circ}$ and 35°, assuming 1 ms coherent integration time, 14500 incoherent averages, and typical satellite transmited powers (modified from [25]).

Altimetry precision [cm_{rms}]	σ_h @ $\theta_i = 35°$	σ_h @ $\theta_i = 0°$
Level – 1 Lower band (L5+E5)	L5: 56.0	L5: 29.7
LB = 1186.6 MHz	E5: 15.5	E5: 8.3
Level 1 – Higher band (L1 + E1)	L1: 37.2	L1: 16.4
LH = 1575.42 MHz	E1: 26.6	E1: 12.8
Level 2	L1&L5: 60.5	L1&L5: 30.5
(LB + LH + ionospheric corrections)	E1&E5: 27.7	E1&E5: 13.7

As it will be shown, the estimated EM bias is on the order of magnitude of the expected rms altimetry precision.

In this Ph.D. Thesis, the GNSS-R bistatic radar equation has applied and simulated. When the wind-driven waves on the sea surface, the diffuse scattering of the GNSS L-band signal is created by the quasi-specular reflections on curved facets produced by waves [29]. By considering type of scattering, a bistatic radar equation was proposed for GNSS-R application using the Delay-Doppler Map (DDM) and the Woodward Ambiguity Function (WAF) [30], [31] (section 1.6).

1.3- GNSS Systems

GNSS systems include three main segments: the space segment, the control segment, and the user segment. The space segment of the GPS consists of satellites in Medium Earth Orbit (MEO) at height of 22000 km, and the control segment is placed on the ground for control and monitoring the satellite constellation and updating procedure. The user segment consists GNSS receiver to give the Position, Velocity and Time (PVT) to the user at all over the world at all time (at least four satellites are in view of user).

The first generation of positioning systems proposed using 24 satellites, but it was designed for 32 satellites, the rest are spares. The GPS satellite is broadcasting in L1 (1.57542 GHz), L2 (1.22760 GHz), and L5 (1.17645 GHz) frequency bands in order to compensate for the ionospheric effects for civilian and military applications. The GPS L1 band has become the most significant band for navigation purposes.

The space segment consists of the satellites constellation, which are distributed in the several orbits. Each satellite is equipped with navigation payload, a precise atomic clock, a navigation antenna etc. The satellites are located in orbits where at least four satellites are visible continuously all over the world with the best geometric dilution of precision (GDOP). The MEO layer is selected because of the larger coverage from a far distance.

An upcoming generation of LEO satellites orbiting below the GPS satellites, can use the GNSS signals for altimetry. A multistatic scenario of GNSS signal application is illustrated in Figure 1.2.

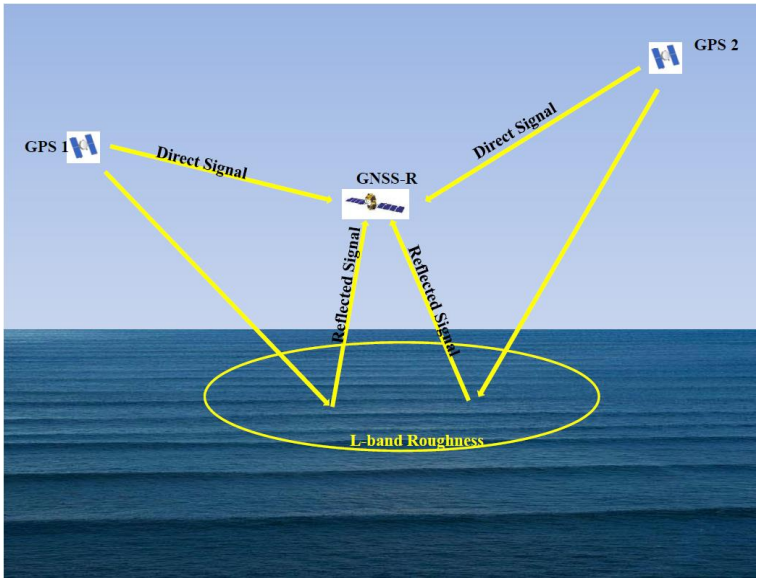

Figure 1.2 Multisatic scenario for GNSS altimetry.

1.4- GNSS signal

Among the different GNSS, the GPS signal structure is explained in this Ph.D. Thesis. It is composed of three main parts: the carrier, the navigation data, and the spreading sequence. The GPS data are broadcasted using an L-band carrier, and the navigation data includes the satellite orbits, which are uploaded to all satellites from the ground station systems. Each satellite has two unique spreading codes, Coarse Acquisition (C/A), and an encrypted one Precision Code (P(Y)) [32]. As mentioned, the navigation data is modulated with carrier wave and codes, the signal transmitted from the k satellite is described as [32] :

$$S^k(t) = \sqrt{2P_c}\left(C^k(t) \oplus D^k(t)\right)\cos(2\pi f_{L1}t) + \sqrt{2P_{PL1}}\left(P^k(t) \oplus D^k(t)\right)\sin(2\pi f_{L1}t) + \sqrt{2P_{PL2}}\left(P^k \oplus D^k(t)\right).\sin(2\pi f_{L2}t), \quad (1.6)$$

where, k is the number of satellite, P_c, P_{PL1}, P_{PL2} are the power of the signals with the C/A or P codes, $C^k$is the CA code sequence assigned to satellite k, P^k is the P(Y) code sequence assigned to satellite number k, D^k is the navigation data sequence, $\oplus$ is the sign of module two adder. The C/A code is selected because of some particular properties such as, each C/A code does not have any cross-correlation to each other's, and all C/A code or the Pseudo-random Noise (PRN) just has correlated value in zero lag. The complete list of the properties are given [32]:

Cross-Correlation

$$r_{ik}(m) = \sum_{l=0}^{1022} C^i(l)C^k(l+m) \approx 0 \qquad for\ all\ m, \tag{1.7}$$

Autocorrelation

$$r_{kk}(m) = \sum_{l=0}^{1022} C^k(l)C^k(l+m) \approx 0 \qquad for\ |m| \geq 1\,, \tag{1.8}$$

where, C^k and C^k are codes from two different satellites. The above-mentioned properties have been simulated in Figure 1.3.

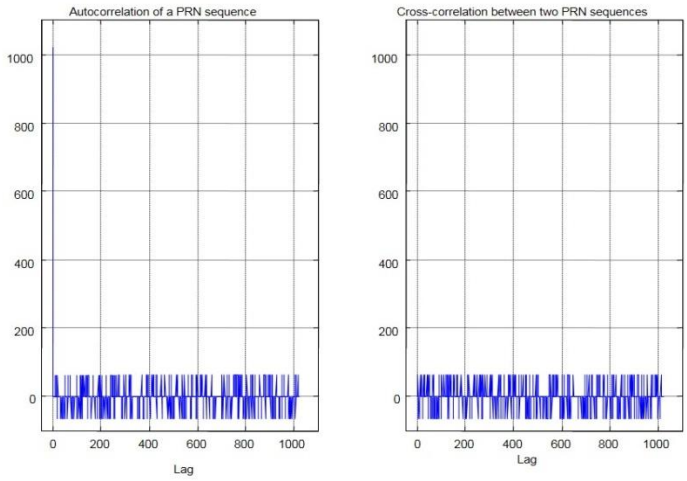

Figure 1.3 PRN code properties, (left) Autocorrelation of a PRN 11 code, (right) Cross-Correlation between two PRN codes (11, 15).

Logically, 32 PRN codes should be generated, it means each satellite has a unique PRN or C/A code. Each C/A code has 1023 chips, and the chip length is $1\frac{ms}{1023} = 977.5ns \approx 1\mu s$.

GPS navigation data has a 1500 bit-long frame, divided in 5 sub-frames, each frame with 300 bits length. Each sub-frame contains 10 words, and each word has a length of 30 bits. Sub-frame one contains the satellite clock and health data, and sub-frame two and three contain satellite ephemeris data, sub-frames four and five contain the almanac data, Universal Time Coordinated (UTC), and ionospheric parameters. Sub-frame 10 begins by two particular words, the telemetry (TLM) and handover word (HOW). TLM is used in frame synchronization. A complete GPS navigation data has a length of 12.5 minutes. The navigation data are transmitted at a rate of 50 bps. An entire GPS navigation data structure is shown in Figure 1.4.

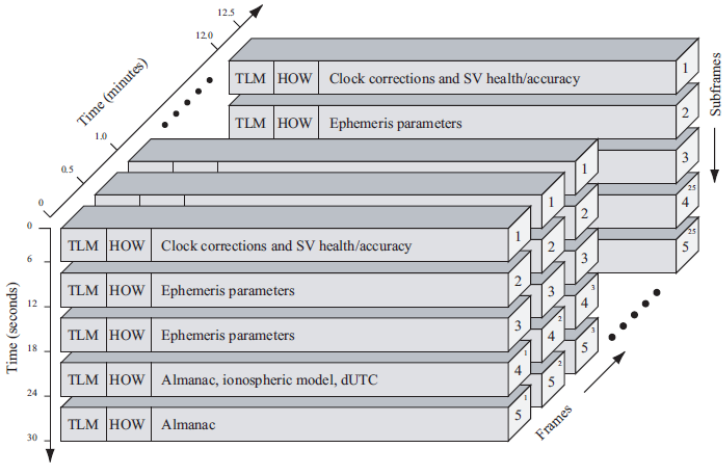

Figure 1.4 GPS Navigation Data Structure [32].

1.5- GNSS Receiver

All GNSS receivers have typical structure that contains: an antenna, a Microwave chain (RF filter, RF amplifier, IF amplifier), and analog-to-digital converter, and software segments: acquisition and tracking module. An schematic GNSS receiver structure is shown in Figure 1.5.

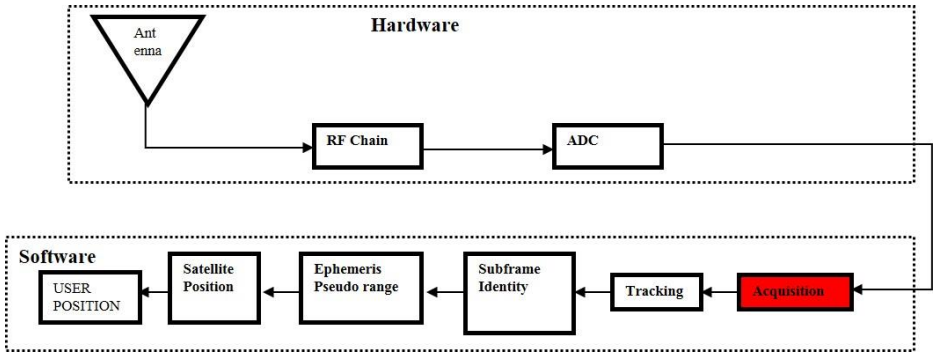

Figure 1.5 GNSS receiver block diagram.

First, incoming wave (direct or reflected GPS wave) from a GNSS antenna (RHCP or LHCP) filtered by band-pass filter (BPF) and amplified then it is converted to an IF band and it is amplified. Here, a GPS signal at L-band is collected using commercial hardware (Appendix B) as explained in the last section and it is presented in Figure 1.6(a). Then, that is filtered by the BPF, which is shown in Figure 1.7, in Figure 1.6(b), the filtered wave have displayed clearly.

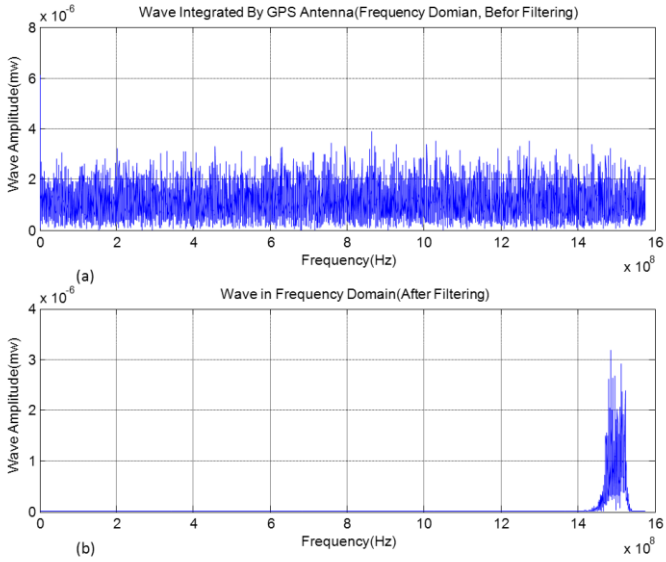

Figure 1.6 Integrated GPS signal by GPS antenna (Time Domain), the GPS signal after the Band-Pass Filter (in frequency domain).

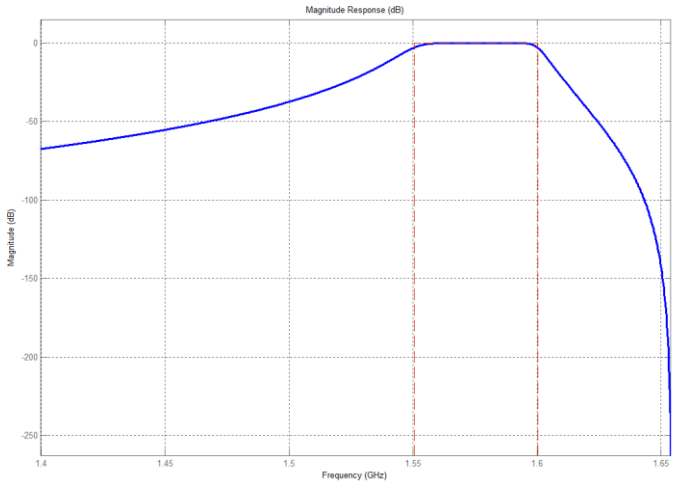

Figure 1.7 BPF filter used in the GNNS receiver simulator.

The software part includes two major modules: acquisition, and tracking (Figure 1.5). In the acquisition module, the visible satellites are indicated using the frequency and code phase (detail on [32]). The parallel code phase search has been selected among several acquisition methods and this module is simulated in this Ph.D. Thesis because of the minimum execution and simulation time. The parallel code phase search algorithm performs a circular correlation through Fourier transform to detect the presence of an incoming PRN signal. For example, the Delay-Doppler Maps (DDM) of PRN 11 is obtained and presented in Figure 1.8. Actually, a real GPS signal was recorded (details in section 1.6 and Appendix B).

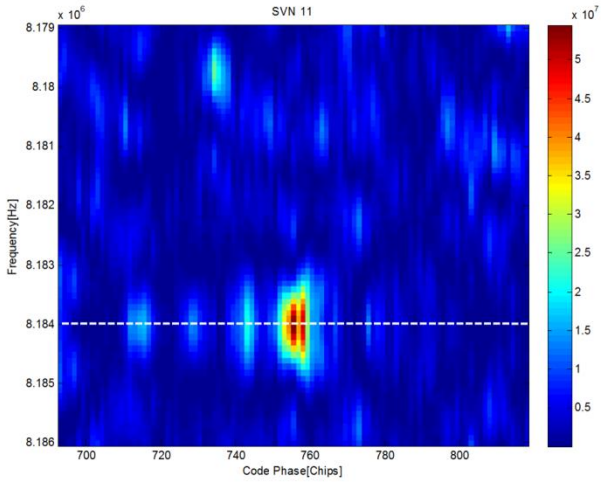

Figure 1.8 Sample DDM obtained from PRN 11extracted from recorded GPS signal.

The tracking module contains two main blocks, code tracking and carrier tracking that is shown in Figure 1.9. Refining the coarse code values of code phase and frequency are the main objectives of tracking module. The code traking and carrier tracking are performed by the DLL and PLL loops, respectively.

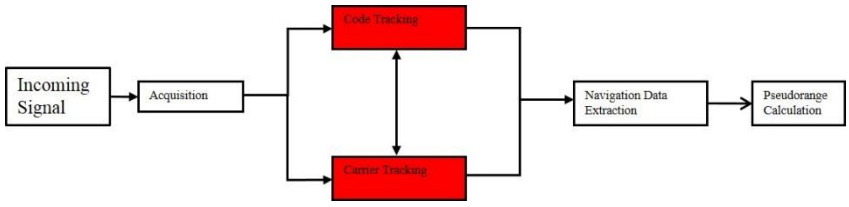

Figure 1.9 Software blocks of GNSS receiver.

Each GPS receiver tracks the PRN code using a Delay Lock-Loop (DLL) and a Phase Lock-Loop (PLL) to maximize the cross-correlation between the incoming code and the one replicated locally. Other research groups have focused on software-based receiver to investigate the reflected GPS signal

(time-delay receiver) in [29], [33], [34]. It contained a RHCP, and a LHCP antenna to record the direct and reflected GPS signals at the same time.

1.6- Retrieving the Sea Surface Profile Using GNSS Signal

As already mentioned, GNNS-R has become a useful technique in remote sensing field. In fact, it used the same technical concept of conventional remote sensing. When the GPS signal is illuminating the Earth's surface (in our case just the ocean surface is considered), the sea surface can scattered some percentages or reflected. Several valuable studies have performed to using GNSS-R in remote sensing [29], [33], [34], [25], [35]–[37].

From a theoretical viewpoint, the scattered GPS wave arriving at the receiver position ($\hat{R}_r$) can be modeled by integral over the mean sea surface Figure 1.10 [33]:

$$u(\hat{R}_r, t) = \int D(\bar{\rho})\, a\left\{t - \frac{[R_0(t) - R(t)]}{c}\right\} g(\bar{\rho}, t) d^2t, \tag{1.9}$$

$$g(\bar{\rho}, t) = -\frac{\mathrm{V}(\bar{\rho}) q^2 \exp\{ik[R_0(t) - R(t)]\}}{4\pi R_0 R q_z}, \tag{1.10}$$

where $D(\bar{\rho})$ is the initial footprint of the receiver antenna, and $a(t)$ is the PRN code function. $R_0(t), R(t)$ are the distances from the transmitter and receiver respectively to the specular reflection point. V is the Fresnel reflection coefficient, q is the scattering vector. Finally, the scattered wave during the averaging time T_1 as [33]:

$$\langle |Y(\tau)|^2 \rangle = T_1^2 \int \frac{D^2(\vec{\rho}) \Lambda^2 \left[\tau - \frac{R_0 - R}{c}\right] \left| S\left[\delta f\left(\underset{\rho}{\rightarrow}\right)\right]\right|^2}{4\pi R_0^2 R^2}\, \sigma_{0b}[\, \vec{q}(\,\vec{\rho}\,)\,] d^2\rho\,, \tag{1.11}$$

where Λ, $S[\delta f(\underset{\rho}{\rightarrow})]$ are the autocorrelation function of satellite's PRN code and the Doppler spreading function, also σ_{0b} is the bistatic scattering cross-section of the ocean surface. In fact, the wind has changed scattering cross-section and the waveform respectively. The waveform has two regions, the maximum or peak and the tails. The peak is sensitive to the wind speed intensity, and the tail is dependent on the elevation angle [30].

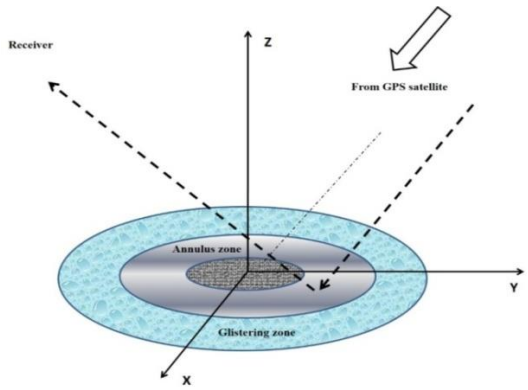

Figure 1.10 GPS scattering geometry.

The three-dimensional DDM of PRN 11 of GPS signal has been computed and it is presented in Figure 1.11. In addition, its waveform and waveform derivative are computed and presented in Figure 1.12.

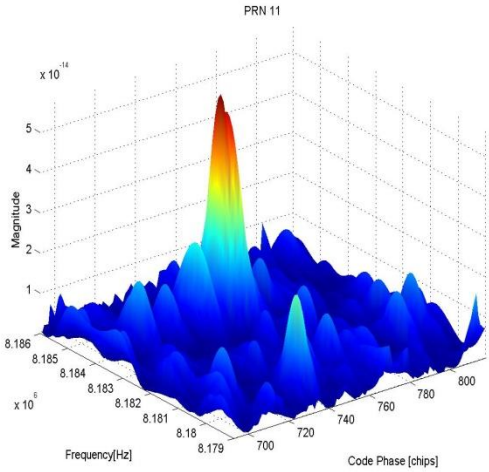

Figure 1.11 Waveform of PRN 11 (from GPS signal).

The waveform derivative is shown that has the delay can be appeared as an electromagnetic bias (Figure 1.12). In GNSS-R altimetry system and scatterometric observation, the shapes of waveforms (reflected one) are used to extract information.

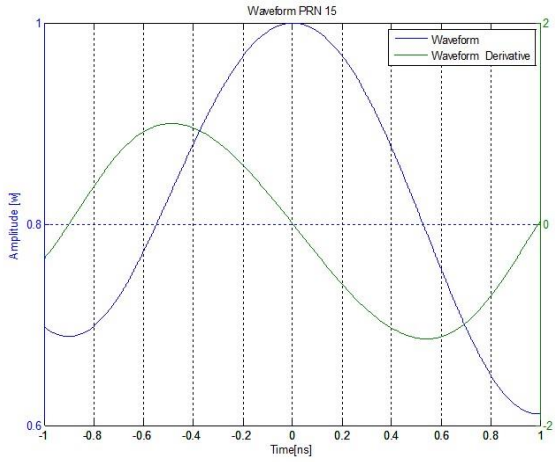

Figure 1.12 Waveform and its derivative from PRN 15.

In this thesis, the reflected GPS waveforms (PRN 11 and 15) are extracted from different sea surface roughness conditions. The different ocean roughness conditions are produced using different wind speeds. The scattered GPS waveforms have been obtained that expressed by increasing the wind speed so the waveform peak became weaker (because at higher wind speed, the sea surface roughness has more roughness so it affected the scattered waves) [15]. Here, it should be mentioned, the reflected GPS waveforms are collected using PO scattering model (Appendix A.2).

1.7- Conclusion

GNSS systems provides a great opportunity for remote sensing, not requiring any dedicated transmitter, and being continuously available. Ocean applications include scattermetry (wind retrieval) and altimetry. For altimetry, L-band exhibites larger EM baises that need to be corrected for upcoming GNSS-R. This study can be helpful for upcoming GNNS-R altimetry missions.

Chapter 2 - Analytical Computation of the Electromagnetic bias in GNSS-R Altimetry

2.1- Introduction

Radar altimeters are used to measure the sea surface topography and the ocean wave height using short radio pulses and measuring the round trip time of travel of the reflected pulses from the ocean surface, and the average reflected power, which is related to the surface scattering cross-section.

In conventional satellite altimetry, the EM bias is one of the most difficult errors to compensate. The EM bias was first reported in [38]. A number of studies on the EM bias have been performed so far for nadir-looking and small off-nadir angles, but because of its significance, it is still a matter of research. In general, there are two approaches to estimate the EM bias: the Weakly Non-Linear (WNL) theory [10], and the Modulation Transfer Function (MTF) model [9]. Jackson [5] applied the WNL theory to estimate the EM bias in one-dimension. In the reflection of radar pulses from the sea surface at near-vertical incidence angles, non-Gaussian ocean wave statistics were accounted for using the joint probability density function (PDF) of the surface's height and slope computed using the Longuet-Higgins theory [39]. The nature of the altimeter's response to a rough sea surface was also an object of research in [5], [11], [12].

GNSS-R was originally proposed for scatterometry in 1988 [40]. Nowadays, one of the promising applications of GNSS-R is mesoscale altimetry, originally proposed in 1993 [1] using the Global Positioning System (GPS) signals.

Most studies on the EM bias have focused on the nadir looking configuration only. Few studies have addressed the off-nadir EM bias estimation using the above-mentioned methods [7], [9], [11], [12]. An analytical method to estimate the EM bias combining both the WNL and the MTF methods was proposed in [13], [14], and validated at Ku-(14 GHz) and C-(5.2 GHz) bands. It showed that the EM bias is dependent on the incidence angle, and that it increases at lower frequencies.

As discussed in chapter 1, wave's asymmetry is responsible for the so-called electromagnetic bias the sea surface height estimation. In the first EM bias studies, the Kirchhoff threshold under the GO approximation was used to compute the scattering cross-section. Using the GO scattering model, Barrick and Peak proposed [41] a proportional relationship between the scattering cross-section, and the ocean roughness statistical parameters in [41]. To determine the statistical parameters, additional assumptions were applied such as in the WNL theory [42].

Latter, considering the short and long waves of the ocean surface roughness, the MTF was applied to estimate the EM bias more precisely, by accounting for the short wave and long wave interactions.

The estimation of the EM bias for a two-dimensional surface using the WNL theory was proposed in [6], [43], although it is applicable only for long waves. To overcome the previous limitations, in [10] a modified WNL theory was proposed to estimate the EM bias applying a unified directional sea surface spectrum that was able to account for long and short waves [8].
Later, an analytical model to compute the EM bias was also studied based on the two-dimensional hydrodynamic modulation [9]. The strong point of the hydrodynamic modulation theory relies on the linearization of the wave action

balance equation. This linearization yields to the so-called modulation transfer function or MTF. In the Fourier domain, the MTF is a function of both the long and the short wave-numbers, and it has also been used to estimate the EM bias in two-dimensional surfaces [9].

The EM bias for a monostatic configuration and for small off-nadir incidence angles was considered in [11], [12], and more recently in [13], [14] using a combination of the WNL and MTF models. In [13] a theoretical formula using some assumptions was proposed that shows that the EM bias depends on the incidence angle, and demonstrated it experimentally.

Both mentioned models have been applied to nadir-looking altimeters. Among exiting EM bias methods (WNL, MTF, and combined model), the combined model [13], [14] is chosen to investigate the EM bias at C- and Ku-bands. In addition, the combined model was also used in off-nadir looking altimeters and it was validated experimentally.

2.2- The Weakly Non-Linear model

The KA-GO method was implemented [5] to compute the scattering cross-section, which was proportional a fraction of the sea surface statistics parameters (the joint PDF). The sea surface was described by a joint PDF Longuet-Higgins [42]. Then it was developed in [6] for a two-dimensional area. An improved WNL method to estimate the EM bias was proposed in [10]. Using the ocean surface statistics the modified EM bias could be estimated as [8]:

$$\beta_{EM} = \frac{\iiint \xi\ \sigma^0 P_L(\xi, \xi_x, \xi_y) d\xi d\xi_x d\xi_y}{\iiint \sigma^0 P_L(\xi, \xi_x, \xi_y) d\xi d\xi_x d\xi_y}, \qquad (2.1)$$

where ξ, ξ_x, and ξ_y are the sea surface height and its slopes over X and Y-axis, and P_L is the joint PDF (roughness and slopes over both axis) defined by as a Gram-Charlier approximation [10]:

$$P_L(\xi, \xi_x, \xi_y) = \frac{G_{1-D}(\eta)}{\sqrt{k_{200}}} \frac{G_{2-D}(\eta, \eta_x, \eta_y; \lambda_{011})}{\sqrt{k_{020}k_{002}}}.$$

$$\left[1 + \frac{\lambda_{300}}{6} H_{300} + \frac{1}{2}(\lambda_{120}H_{120} + \lambda_{102}H_{102} + 2\lambda_{111}H_{111})\right]. \quad (2.2)$$

The H_{ijk} functions are the generalized Hermit polynomials of the normalized variables:

$$\eta = \frac{\xi}{\sqrt{k_{200}}}, \quad (2.3)$$

$$\eta_x^L = \frac{\xi_x}{\sqrt{k_{020}}}, \quad (2.4)$$

$$\eta_y^L = \frac{\xi_y}{\sqrt{k_{002}}}, \quad (2.5)$$

and k_{200} is the variance of the sea surface, k_{020} , k_{002} are the variances of the sea surface slopes, λ_{102} , λ_{120} , λ_{111} are skewness coefficients of the sea surface height and its slopes [6], [8]:

$$\lambda_{mnp} = \frac{k_{mnp}}{k_{200}^{m/2} + k_{020}^{n/2} + k_{002}^{p/2}}. \quad (2.6)$$

Here, the scattering cross-section is assumed to be equal to the sea surface slopes joint PDF and it was rewritten as [10]:

$$\beta_{EM} = \frac{\iiint \xi\, P_S(\xi_x,\xi_y) P_L(\xi,\xi_x,\xi_y) d\xi d\xi_x d\xi_y}{\iiint P_S(\xi_x,\xi_y) P_L(\xi,\xi_x,\xi_y) d\xi d\xi_x d\xi_y}. \quad (2.7).$$

The joint long PDF was combination of 1D and 2D Gaussian PDFs, then the triple integral in (2.1) reduces to a double integral over the slopes components only:

$$\beta_{EM} = \frac{\iint P_S(\xi_x, \xi_y) G_{2-D}^L Q_{2-D}^L(\eta_x^L, \eta_y^L)\, d\xi_x d\xi_y}{\iint P_S(\xi_x, \xi_y) G_{2-D}^L d\xi_x d\xi_y} \cdot \sqrt{k_{200}}, \quad (2.8)$$

where the long wave tilting factors, G_{2-D}^{L} and Q_{2-D}^{L} are the two dimensional Gaussian PDFs and the long wave coupling due to the non-linear statistics:

$$G_{2-D}^{L} = \frac{1}{\sqrt{k_{020}k_{002}}}\, G_{2-D}(\eta_x^L, \eta_x^L; \lambda_{011}), \tag{2.9}$$

$$Q_{2-D}^{L} = \frac{1}{2}\,\lambda_{120}H_{20}(\eta_x^L, \eta_x^L; \lambda_{011}) + \frac{1}{2}\,\lambda_{102}H_{02}(\eta_x^L, \eta_x^L; \lambda_{011}) + \frac{1}{2}\,\lambda_{111}H_{11}(\eta_x^L, \eta_x^L; \lambda_{011}), \tag{2.10}$$

$$P_S(\xi_x, \xi_y) = \frac{1}{\sqrt{k_{20}k_{02}}}\, G_{2-D}(\eta_x^S, \eta_x^S; \lambda_{11}), \tag{2.11}$$

$$\eta_x^S = \frac{\xi_x}{\sqrt{k_{20}}}, \tag{2.12}$$

$$\eta_y^S = \frac{\xi_y}{\sqrt{k_{02}}}, \tag{2.13}.$$

where the slopes components are normalized by the rms slope of short waves and k_{20}, k_{02} are variance of slopes. From a snapshot of the sea surface roughness that joint PDF histogram is obtained and illustrated Figure 2.1.

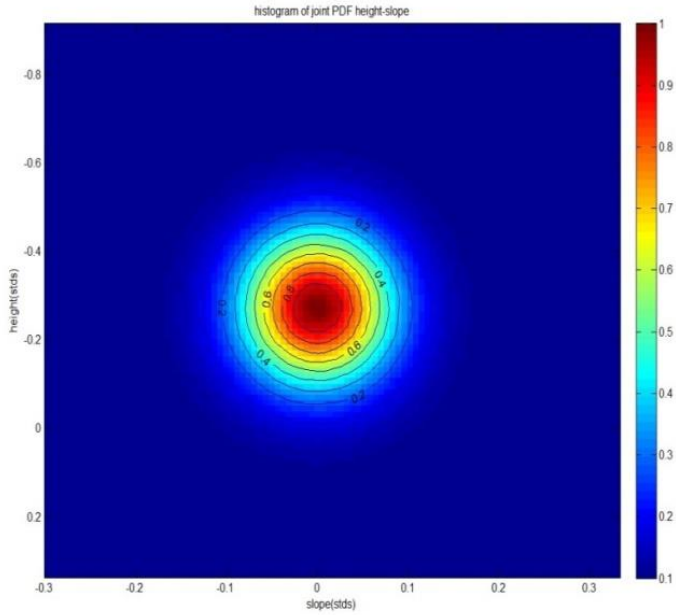

Figure 2.1 Gram-Charlier PDF from long wave components.

The EM bias is estimated using [6] and [10] the KA-GO method to compute the scattering cross-section. Results are shown in Figure 2.2. It should be emphasized the KA-GO scattering method is simulated in the simulation part and explained in appendix A.1 comprehensively.

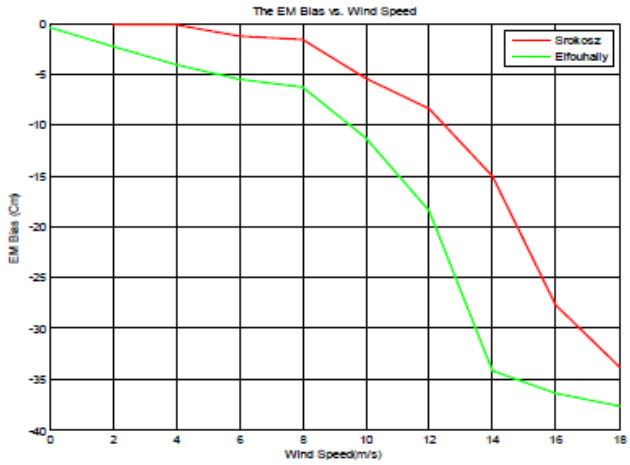

Figure 2.2 The EM bias vs. wind speed computed using the WNL theory Srokosz [3], and Elfouhaily [7].

In the KA-GO method, the radar cross-section σ^0 is proportional to the slope's PDF of the short waves, which can be expressed in terms of the local tilting over the long waves.

2.3- Modulation Transfer Function Method

The modulation of short waves height is a function of the sea surface displacement, which causes a differential in the seas surface roughness between the crests and troughs. The MTF model was developed, to describe the interaction between long and short waves [44].

The correlation between nadir-looking radar cross-section and surface elevation is related to the local short wave statistics [45], which was applied the MTF model. On the other hand, based on the KA-GO method, the ocean surface radar-cross sections under nadir looking can be computed by multiplication of the short-wave PDF and a geometric correction of the local tilting angle [41]. The relationship between the radar cross-sections was

already shown to be the sum of the relative variation of the sea surface elevation and its slopes [9]. Generally, this method can be used in rough surfaces with average radius of curvature much larger than the electromagnetic wavelength [46]. Usually the radius of curvature the ocean surface is on the centimetre range. Therefore, the KA-GO assumption is not acceptable, and as a consequence, the standard method was proposed, which assumed the sea surface "seen" after being filtered [47]. The sea surface curvature or its slopes are functions of the high-frequency part of the sea surface spectrum [41], [48]. At small wave modulation with large modulation a Wentzel-Kramers-Brillouin (WKB) approach is applied in [44]. The fundamentals of this method are based on the hydrodynamic modulation theory of the wave action balance equation, or MTF. The MTF in the Fourier domain is a function of both the long and the short wave numbers [44]. The modulation of wave spectrum in the Fourier domain is given by:

$$\frac{\delta\psi}{\psi_e} = \int R(K_L, K_S) Z_{KL}\, e^{-(K_L.r-\omega_L.t)} dK_L + c.c.\,, \qquad (2.14)$$

where, $R(K_L, K_S)$ is the MTF, K_L, K_S are wave numbers of the short and the long waves components, Z_{KL} is the Fourier transform of the elevation of the long modulation waves, ψ_e is the equilibrium spectrum of short waves, and c.c. is a complex integration constant .

In fact, variations of the radar cross-sections are mainly caused by the long-wave tilting. The hydrodynamic modulation applies variation in the short-wave statistics along the phase of the long-waves. Based on the above definition, the EM bias can be divided into two components (Elfouhaily, et al., [9]):

$$\beta_{EM} = \frac{\langle \xi\, \widetilde{\sigma^0} \rangle}{\langle \sigma^0 \rangle} \triangleq \beta_T + \beta_H\,, \qquad (2.15)$$

where β_T and β_H are the tilt and the hydrodynamic biases. It should be mentioned that the tilt bias exists only under the condition of non-linear statistics; if the long-wave modulation is linear, then the tilt bias is zero. The tilt bias can be decomposed into the first order tilt bias, which is a function of the cross-skewness of the sea surface and its slopes, and the second order is function of higher-order statistics (e.g. kurtosis) between the sea surface elevation and its slopes (Elfouhaily, et al., [49]).

2.3.1- Modulation of the Radar Cross Section:

Based on the KA-GO model [41], [48], the ocean surface radar cross-section at nadir incidence angles is proportional to the short-wave PDF $P_s(X_L)$ times a geometric correction $T(X_L)$ of the local tilt angle [9]:

$$\sigma^0 \propto PDF_s(X_L)T(X_L)\,, \tag{2.16}$$

where X_L is the surface's slope, and the radar cross-section σ^0 can be represented as a sum of relative variations of slope moments [16]:

$$\frac{\delta\sigma^0}{\sigma^0} = f_{20}\frac{\delta k_{20}}{k_{20}} + f_{11}\frac{\delta k_{11}}{k_{11}} + f_{02}\frac{\delta k_{02}}{k_{02}}\,, \tag{2.17}$$

where k_{20}, k_{11}, k_{02} are the cumulants of the surface distributions, and f_{20}, f_{11}, f_{02} are revealing a binomial dependence on the moment vector (details in [16]).

2.4- Combined EM Bias Model

In the combined EM bias model [13], the two previous models are used to estimate the EM bias. In fact, the sea surface roughness is assumed to be split in two models (long and short waves), the sea surface is generated using the synthesized spectrum proposed in [50], then the KA-PO scattering method was used to obtain the scattering cross-section. In this model, the short-wave EM bias is estimated using the MTF model and the long-wave EM bias

computed using the Gram-Charlier series. In this Ph.D. thesis, this combined model is simulated at C and Ku bands and validated. In fact, the combined model is used to compute the EM bias at L-band and published that is related to GNSS systems [51], [52]. Few studies on the EM bias for off-nadir incidence angles have been reported [11], [12], [13], [14]. The bistatic radar cross-section [53], has a relatively weak cosine dependence with the incidence angle, that will have influence the EM bias. Experimental and theoretical studies have confirmed that the EM bias depends on the incidence angle. In that work, the radar cross-section was computed by the MTF of short waves. Finally, based on the general definition of the EM bias, the EM bias for off-nadir incidence angles can be estimated by combining both the WNL theory and the MTF model. The EM bias computed from [13] is expressed as:

$$\epsilon = \frac{\iint \xi \sigma^0(\xi, \theta + \theta_l) P(\xi, \theta) d\xi d\theta_l}{\iint \sigma^0(\xi, \theta + \theta_l) P(\xi, \theta_l) d\xi d\theta_l}, \tag{2.18}$$

where σ^0 and ξ are the radar cross-section, and the sea surface height, θ is the incidence angle relative to the mean sea surface, θ_l is the local long-wave tilt angles, and $P(\xi, \theta)$ is the joint long-wave height distribution, which can be expressed as a Gram-Charlier series [6], [10]:

$$P(\eta, \eta_x) = \frac{e^{-\frac{1}{2}(\eta^2 + \eta_x^2)}}{2\pi h_l S} \left\{1 + \frac{\lambda_{30}}{6} H_{30}(\eta, \eta_x) + \frac{\lambda_{12}}{2} H_{12}(\eta, \eta_x)\right\}, \tag{2.19}$$

where, η, η_x are the sea surface elevation and its slope relative to x, and λ_{30} , λ_{12} are the cross skewness of the sea surface and its slope, H_{30}, H_{12} are the Hermit polynomial functions, $h_{l,}$ and S are the standard deviation of the long waves and their slopes:

$$\lambda_{30} = \frac{E[\xi^3]}{E[\xi^2]^{3/2}}, \tag{2.20}$$

$$\lambda_{12} = \frac{E[\xi^3 \xi_x^2]}{E[\xi^2]^{1/2} E[\xi_x^2]}, \tag{2.21}$$

$$H_{30}(\eta, \eta_x) = \eta^2 - 3\eta, \tag{2.22}$$

$$H_{12}(\eta, \eta_x) = \eta\ (\eta_x^2\ - 1). \tag{2.23}$$

The radar cross-section is related to the small waves by the MTF. The strength of the hydrodynamic modulation can be presented as the normalized correlation between the short waves and the long waves in [45]. The final analytical formula for off-nadir incidence angles can then be presented as [13]:

$$\epsilon(\theta) = -H[\gamma(\theta).\nu.S + \tau(\theta).\lambda_{12}], \tag{2.24}$$

where, ν is constant (Kinematic velocity of air), $\gamma(\theta)$, and $\tau(\theta)$ are small wave coefficients, which are can be determined by an isotropic unidirectional power law surface height spectrum:

$$\gamma(\theta) = -\frac{1}{2}\frac{\iint \lambda_0(1-C)e^{i2k_{em}x\theta}e^{-\lambda_0(1-C)}e^{-\mu^2/2}dxdy}{\iint e^{-\lambda_0(1-C)}e^{-\mu^2/2}dxdy}, \tag{2.25}$$

$$\tau(\theta) = +\frac{1}{8}\frac{\iint e^{i2k_{em}x\theta}e^{-\lambda_0(1-C)}e^{-\mu^2/2}dxdy}{\iint e^{-\lambda_0(1-C)}e^{-\mu^2/2}dxdy}, \tag{2.26}$$

$$\mu = 2xk_{em}s_l, \tag{2.27}$$

$$\lambda_0 = (2k_{em}h_0)^2, \tag{2.28}$$

where, k_{em} is the electromagnetic wave number, C is the Fourier transform of the isotropic short wave power spectral density, s_l^2 is the surface's slope variance, and h_0 is the average short wave height variance.

Using a cut-off wave number in the current model is used to provide more accurate method of the scattering from small waves on the order of the electromagnetic wave length in size. Based on the experimental results, with increasing incidence angle [13], it was shown that the sharp crests produce a larger backscatter than the flatter valleys, but the sign of the bias changes. Finally, by using the bistatic radar cross-section of KA-GO scattered field is proposed [13]:

$$\sigma^0 = k\ cos^2\theta \exp\left[\frac{-k_b^2}{2x^2|G|}\right], \tag{2.29}$$

where: $|G|$ is normalized slope variance, and k_b is the Bragg-scattering wave number. Now, the radar cross-section is used to estimating the EM bias, So, the EM bias for off-nadir incidence angles can be studied more accurately in GNSS-R system. The EM bias combined model is simulated for several incidence angles, that are described in next chapter.

2.5- Conclusions

The EM bias is one of the most tricky errors to assess in radar altimetry. The EM bias can be estimated by different theories such as the WNL, or the MTF. Results using both are presented here for inter-comparison purposes and to validate the numerical method that will be presented. By applying both theories to estimate the EM bias at off-nadir incidence angles, the incidence angle dependence can be assessed. The interesting result is the EM bias dependence on wind intensity obviously mimics the radar cross-section behavior.

Chapter 3 - Numerical Computation of Electromagnetic Bias in GNSS-R Altimetry

3.1- Introduction

In this chapter the EM bias is computed using numerical simulations. To do so, a time-dependent synthetic non-Gaussian sea surface is created using the Pierson-Moskowitz and Elfouhaily sea surface height spectra and spreading function. The sea surface is then discretized in facets and "illuminated" using a Right Hand Circular Polarization (RHCP) GNSS signal, previously recorded by an up-looking antenna connected to a data logger. The waves scattered from each facet are then computed using the Physical Optics (PO) method under the Kirchhoff Approximation (KA) (Appendix A). The scattered electric fields are "collected" by a down-looking Left Hand Circular Polarization (LHCP) antenna, and the electromagnetic bias (EM bias) is computed based on its fundamental definition. The numerical model is validated against Millet's model (a combined model of the Weakly Non-Linear and Modulation Transfer models) at C- and Ku-bands, and with the limited real data existing (see chapter 2). Then, the numerical model is applied at L-band, for bistatic configurations, including different azimuthal angles, and different wind speeds. It is found that the EM bias is almost insensitive to the sea surface spectra selected and increases with increasing incidence/scattering angle, and wind speed, and it also exhibits a non-negligible azimuthal dependence, that must be accounted for in the error budgets of upcoming GNSS-R altimetry missions.

The signal received by a down-looking left-hand circularly-polarized (LHCP) antenna is computed as the sum of the different contributions from the

different scatterers properly weighted by the co- and cross-polarization antenna patterns.

3.2- Simulation Approach

Recently, a Monte-Carlo study on the EM bias has been performed using non-linear numerical hydrodynamic simulations [54], and applying the KA PO method to simulate the scattered signal [55]. This work showed a non-negligible impact of the short waves on the EM bias for different frequencies, and a nadir-looking configuration in a one-dimensional scale.

In this work, in order to assess the impact of the particular sea surface spectra, the Pierson-Moskowitz and the Elfouhaily spectra, are used to generate the sea surface [50], [56], including the spreading function (the up-wind and cross-wind asymmetry) [57]. The non-linearity of the generated sea surface is assessed in [58]. The surface is illuminated by a GPS signal, the scattered wave is computed using KA-PO method because of its higher accuracy, from which the scattering cross-section is estimated [19, 20, 27, 28].

Millet's method (combined WNL and MTF, chapter 2) has been implemented and validated with higher frequency data (C- and Ku-bands), first. Then, the method is applied to the calculation of the EM bias at L-band for off-nadir incidence angles such as in GNSS-R systems, and results at L-, C-, and Ku-bands are compared to the numerical technique proposed in this work. Once the numerical model is validated, the obtained EM bias is computed as a function of the wind speed, incidence/scattering, and azimuth angles. The proposed method is numerically efficient and stable, and it requires a modest number (10) of Monte-Carlo simulations to provide statistically meaningful results.

This work is organized as follows. Section 3.2 gives the background for the EM bias computation, the generation of the non-Gaussian sea surface, and the illumination of the generated sea surface by a RHCP (GPS-like) electromagnetic wave, and the computation of the scattered wave using the KA-PO. In Section 3.3, the off-nadir EM bias combined model (WNL+MTF) is validated at C- and Ku-bands, and then applied at L-band. Section 3.4 presents the results of the numerical method proposed, which are validated against the combined model, and discusses them as a function of the sea surface spectra model, frequency band (L- C-, and Ku-band), surface discretization, wind speed, incidence/scattering and azimuth angles. Finally, Section 3.5 summarizes the main conclusions.

3.3- EM Bias Computation

In order to estimate the EM bias, three main simulator blocks have to be implemented:

1) the generation of a time-dependent non-Gaussian realistic sea surface,
2) the generation of the RHCP direct signal (in this case a true GNSS signal collected using an up-looking antenna connected to a data logger) that illuminates the sea surface, and
3) the computation of the scattered signal using, for example, the KA-PO method [4, 19, 20, 27]. This method has proven to be quite accurate for forward scattering even for polarimetric studies.

These steps are considered separately in the next sections, after reviewing the existing methods to compute the EM bias.

3.3.1- Summary of Existing Methods to Compute the EM Bias

There are three main methods to estimate the EM bias: the WNL theory [10], the MTF [9], and a combined model (WNL & MTF).

In GNSS-R, the incidence angle may be quite large (35°-45°), and its impact has to be considered. Then, a suitable method to estimate the EM bias has to be derived. Millet's et al. method (combined method) comprised the **improved WNL and** the **MTF model**, was implemented to estimate the EM bias at Ku-band [13], [14]. In this method, the impact of long waves is computed as the contribution of the improved WNL theory, while the impact of short waves is accounted for using the MTF model.

The combined model (WNL + MTF) is validated with real data and it is considered in this work as a reference to estimate the off-nadir EM bias at other frequencies and geometries accounting for the long and short waves EM bias contributions separately [7], [13], [61].
In [13], the off-nadir EM bias model was computed as a function of the long wave surface statistics (Gram-Charlier series [6]), and modified by the small wave coefficient. The small wave coefficient was computed from the short wave surface scattering obtained using the PO method. The incidence angle was included in the computation of the small wave scattering [13].

In the off-nadir EM bias model, the composite surface scattering model used a cut-off wave number k_{sep} to divide the surface into long and short wave scales. Because of the weak sensitivity to k_{sep}, the unified Elfouhaily' spectrum was considered. For short wave scales, the significant slope of spectrum has been used for separation wavelength over a wide range of wind speeds [7], [13], [61].

This combined EM bias model is validated at Ku-band (14 GHz), and C-band (5.2 GHz). It is then extrapolated at L-band (1.575 GHz) for GNSS-R applications, and used for inter-comparison with (validation of) the numerical results obtained later. Results are presented in Section 3.4.

3.3.2- Numerical Computation of the EM bias

The EM bias basic definition is simply the ratio of the average of the radar cross-section density (σ^0) times the sea surface elevation (ξ), divided by the average σ^0 [8]:

$$\beta_{EM} = \frac{\langle \xi\, \sigma^0 \rangle}{\langle \sigma^0 \rangle}, \tag{3.1}$$

To evaluate Eqn. (3.1), the surface wave height and σ^0 are required. The sea surface wave height and orientation for each facet are known, since they are the outputs of the sea surface generator. The value of σ^0 is computed using the KA-PO method (Appendix A.3).

3.3.3- Generation of a synthetic non-Gaussian sea surface

As already suggested, for the assessment of the average EM bias [18] the ocean surface cannot be considered a Gaussian surface. As a matter of fact, wave crests are more peaked than the wave troughs, and this effect translates into a surface height PDF with a non-symmetric behavior, that has a non-zero skewness coefficient [62]. There are several methods to generate a non-Gaussian surface (e.g. [54]), with benefits and drawbacks (mainly the large computational time), that have been investigated in [63].

In this work, two directional sea surface height spectra (Pierson-Moskowitz and Elfouhaily et al.) are selected and then converted to directional spectra using a cosine-shape, and a unified spreading model function, respectively

[50], [56]. In order to assess the non-Gaussianity of the generated surface, the numerical method proposed in [58] is applied here.

A snapshot of the non-Gaussian sea surface is shown in Figure 3.1, using the parameters listed in [50].

Table 3.1 Parameters used to synthesize the (non-Gaussian) time-domain sea surface.

Parameter	Value/Unit
Patch area	1000 x 1000 m^2
Wind Speed	5 m/s
Wind Direction	45°
Sea Surface Spectrum	Elfouhaily et al. [50]
Anisotropic Spectrum	Unified Spreading Function (up-wind/cross-wind asymmetry)

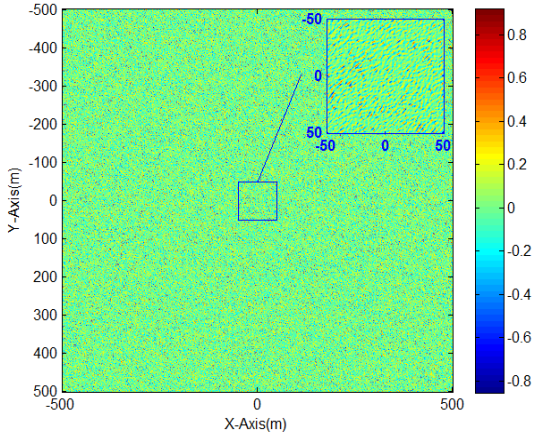

Figure 3.1 Sample of the non-Gaussian sea surface generated using Elfouhaily's spectrum for a wind speed=5 m/s, and wind direction $\varphi = 45^{o}$. Upper right corner: zoom of the central part to better appreciate the wavy structure. Colorbar indicates the sea surface height of each pixel.

Finally, the non-Gaussian surface height PDF is obtained for three different wind speeds 5, 10, 15 m/s, and it is presented in Figure 3.2. The estimated PDF's are similar to the Edge-Worth expansion, demonstrated experimentally and theoretically in [42], [58], [64]–[70], and deviate from the Gaussian model as the wind speed increases.

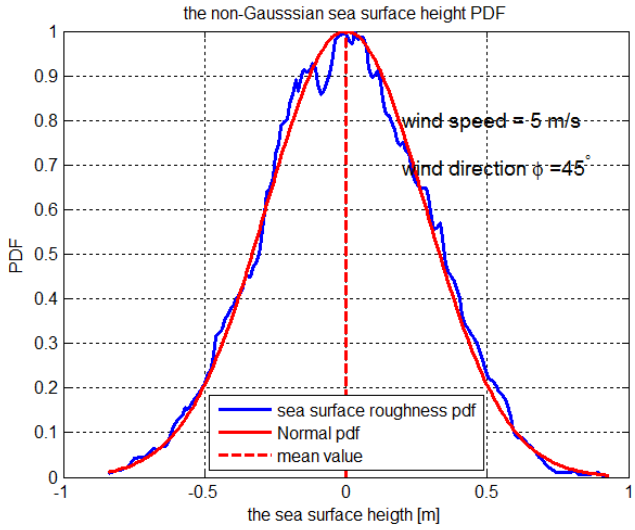

(a)

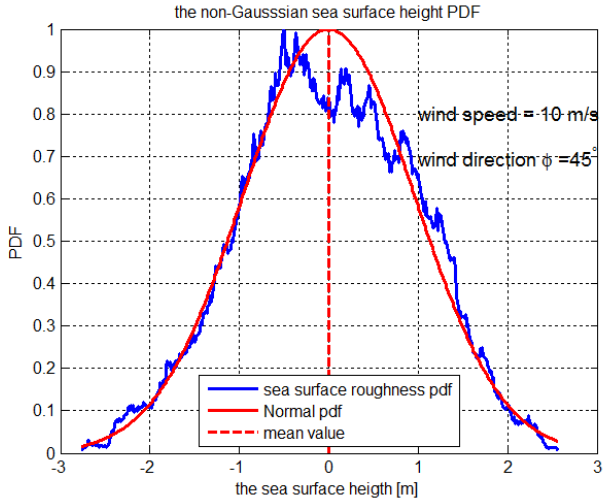

(b)

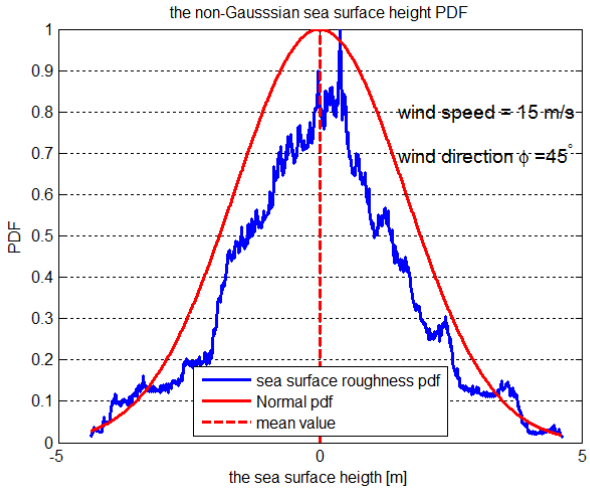

(c)

Figure 3.2 Computed sea surface height PDF (normalized) from 10 realization for different wind speeds (5, 10, 15 m/s). Note that the PDF departs from Gaussian as wind speed increases.

3.3.4- Generation of the direct signal

GPS satellites transmit RHCP waves[3] at L1 (1575,42 MHz), modulated using the Coarse/Acquisition (C/A) code for civilian applications. In order to be more realistic, a direct multipath-free GPS signal recorded using a GPS antenna, an L-band low-noise microwave amplifier, and a data logger.

3.3.5- Computing the Scattered Wave using the Physical Optics (PO) under the Scalar approximation Method

The KA PO method has been implemented in the forward scattering scenario to estimate the EM bias [13], [14], [30], [59] (Appendix A.4, and B). Once the time-domain sea surface (Appendix C, D) is illuminated, the instantaneous scattered field is computed for each facet in which the three-dimensional surface is discretized. Each point of the sea surface is described by its displacement with respect to the flat surface (height), a unit normal vector $\widehat{\boldsymbol{n}_l}$ perpendicular to each facet, where the tilting angle from the $\hat{Z}$ axis is given by $\theta = \arccos(\hat{Z}.\widehat{n_l})$, and the rotation angle φ (see Figure 3.3).

In addition, a finer sea surface discretization is applied to study the impact of short-waves on the radar cross-section. The scattered wave is then computed by summing up coherently all the contributions from all facets.

The basics of the KA model assume that locally the surface can be approximated by an inclined plane. The surface correlation length must be larger than electromagnetic wavelength, and the standard deviation of the

[3]The residual left-hand circularly polarized (LHCP) transmitted signal is neglected for the object of this study.

surface height must be small, so that the average radius of curvature is much larger than the electromagnetic wavelength [30], [60].

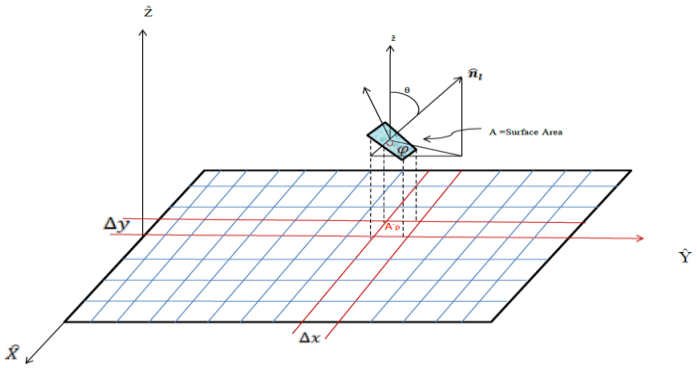

Figure 3.3 Representation of the surface facet discretization.

It has been proven that, at L-band, in a forward scattering scenario[4], even cross-polar terms can be accurately described using the KA-PO method [30], [60]. The facet size height and orientation are discussed (appendix C), and the facet surface is assumed as non-metallic (dielectric constant $\varepsilon_r = 73 + j57.5$) [71]. In this work, the generated sea surface is discretized into facets of an equivalent size close to the electromagnetic wavelength (~20 cm). The validation of this approach is assessed in section 3.4.2.

This procedure is implemented over a square synthetic sea surface of 6 km side, much larger than the electromagnetic wavelength, and then the wavelength of the sea waves, even for strong winds and developed seas. For computational purposes, the surface was divided in blocks of 1000 m x 1000

[4] The scattered wave is mostly LHCP for an incident wave at RHCP.

m each one, discretized in 25×10^6 points, for which each realization (10 Monte Carlo simulations[5]) takes about 27 min in a computer.

3.4- Validating the off-Nadir EM Bias Combined Model

To validate Millet et al. method (combined model) with the few existing data (scatter plot in Figure 3-5 in terms of the significant wave height), the relationship between the significant wave-height and the wind speed has to be obtained first using foe example the Elfouhaily's spectrum (Figure 3.4). This relationship is applied to estimate in the off-nadir EM bias using the combined model at both C-(5.2 GHz) and Ku-(14 GHz) bands, and to compare these results with the few existing experimental data [13] (Figure 3.5).

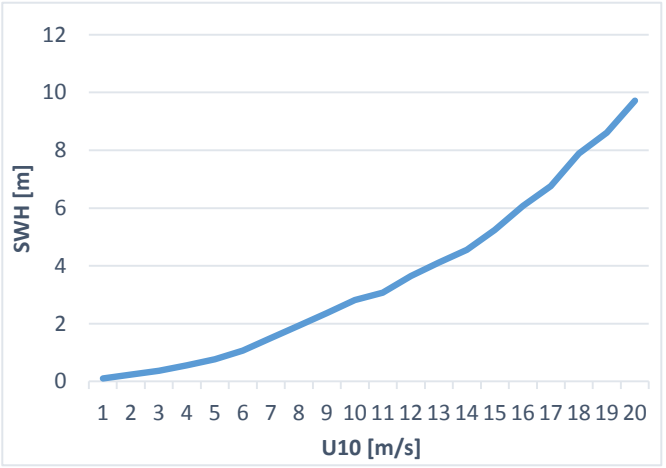

Figure 3.4 Significant wave-height vs. wind speed computed using Elfouhaily et al.'s spectrum [50].

[5] Because of the large spatial accuracy performed, few Monte Carlo are realization are required.

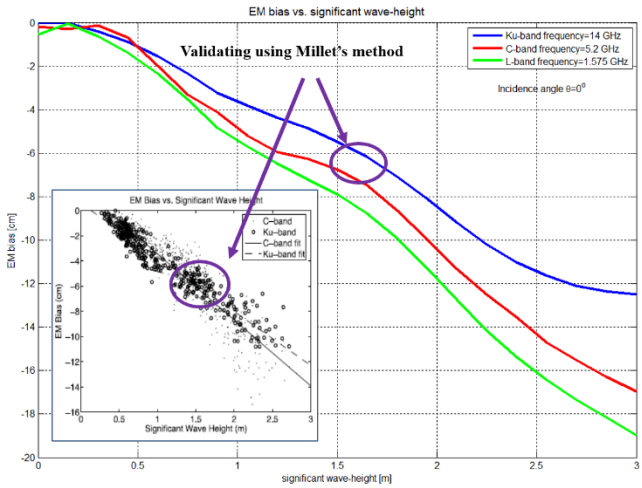

Figure 3.5 The EM bias computed (θ_i=0°) at C- and Ku-band using the combined model, and validation with existing experimental data (scattered plot in subplot on the low left corner from, [11] Figure 8, Eqns. 14, 15).

The agreement between the simulation results and the experimental data is pretty good. Once the implementation of the combined model is validated, the EM bias at L-band (1.575 GHz) can be computed. Results are presented in Figure 3.6, now in terms of the wind speed. At ~12 m/s, the EM bias increases with decreasing frequencies: ~-12 cm at Ku-band, ~-17 cm at C-band, and ~-19 cm at L-band.

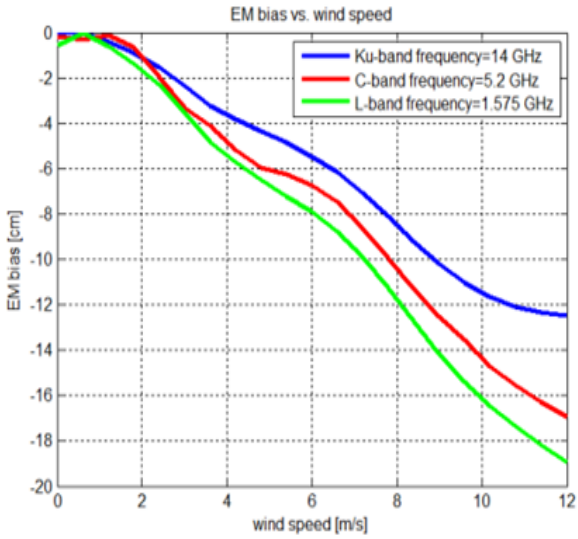

Figure 3.6 EM bias vs. significant wave-height at three difference frequencies obtained using the combined model, the blue and red ones are the same as in Figure 3.5, but with the horizontal axis in terms of wind speed [13], Figure 8, Eqn. 14, 15].

3.5- Simulation Results and Discussion

In this section, results of the EM bias combined model and the numerical method are presented and compared to validate the proposed numerical method, based in the direct evaluation of Eqn. (3.1). Finally, the effect on the EM bias of some parameters such as: the frequency, incidence/scattering angle, wind direction, sea surface height spectra model, and discretization, are investigated using the proposed numerical method and discussed.

3.5.1- Effect of the Sea Surface Height Spectrum

The impact on the EM bias of two both well-known sea surface spectra (Pierson-Moskowitz [62], and Elfouhaily spectra including the spreading

function [50]) is examined using the proposed numerical method for an incidence/scattering angle of 25°, and a wind directions (0°, 45°) (Figure 3.7). Error bars indicate the 95% confidence levels.

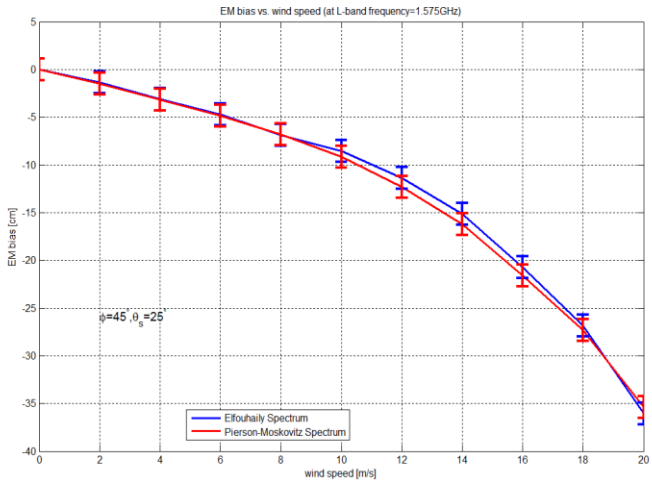

Figure 3.7 Comparison of the EM bias (at L-Band) vs. wind speed using the Pierson-Moskowitz [45] and Elfouhaily et al. spectra (facet size 20 cm) [50].

It is apparent that the trend is similar, and results are very similar, although for moderate wind speed there are differences as high as ~2 cm. The results in Figure 3.7 indicate that the actual sea surface spectrum is not critical. From now on, the Elfouhaily's spectrum is used throughout this work.

3.5.2- Impact of Surface Discretization

The effects of the short-wave components on the radar cross-section have been investigated experimentally in [72], and they have shown that it is nearly independent on the wind speed at near-nadir incidence angles. However, at larger incidence angles, σ^0 increases with increasing wind speeds. In order to investigate the impact of the short-wave components on the EM bias, the

surface is discretized into smaller facets (10 cm side) and compared to the nominal discretization (20 cm side). Simulation results at L-band, wind direction of 45°, incidence/scattering angle of 0° are presented in Figure 3.8.

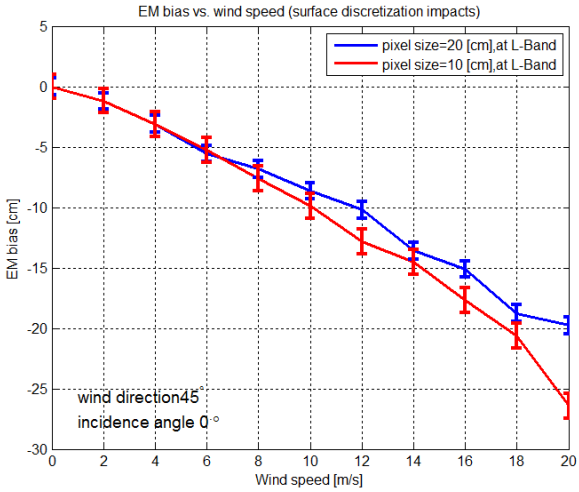

Figure 3.8 Comparison of the sea surface discretization impact on the EM bias (Elfouhaily et al. 's spectra [50]).

As it can be appreciated, the EM bias difference is negligible for very low wind speeds ($U_{10} \leq 6$ m/s), but it increases with increasing wind speeds, the EM bias being larger with the 10 cm discretization, than with the 20 cm one, due to the presence of short wave components: ~2-3 cm up to 18 m/s, and ~6 cm at 20 m/s. However, the largest contribution to the EM bias is coming from the long waves, in agreement with [13].

3.5.3- Investigating the Incidence Angle Impact on the EM Bias

In order to investigate the impact of the incidence angle on the EM bias, the EM bias combined model is used to simulate and investigate several incidence/scattering angles 0°, 25°, and 45° at Ku-band [13], [14] (Figure 3.9).

As the incidence angle increases, the EM bias (β_{EM}) increases as well, approximately as a cosine function. This is due to the extra transit time Δt from transmitter to receiver when the surface is displaced a height h: $\Delta t = 2h/c \cdot \cos\theta$. The EM bias is then computed at L-band using our numerical method for the same incidence/scattering angles 0^o, 25^o, and 45^o (Figure 3.9). The EM bias is larger at L-band than it is at Ku-band, but the trend with incidence angle is similar.

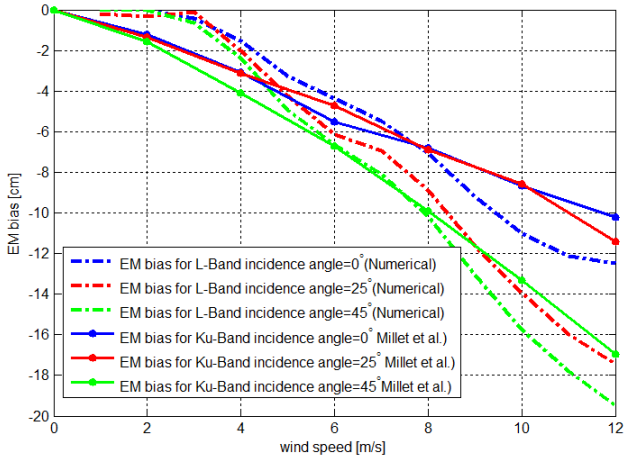

Figure 3.9 Comparison of incidence angle impact on the EM bias at L- and Ku-bands using the combined method (Millet et al. method) [11], [12] and the proposed numerical method. Error bars not included for the sake of clarity.

Estimated EM bias, using the numerical method at L-band are shown with 95% confidence intervals for several incidence angles 0^o, 25^o, 45^o, and with wind direction 0^o (Figure 3.10). As it can be appreciated, the EM bias increases with increasing incidence angles and increasing wind speeds up to ~22 cm for $\phi = 0°$ and θ_s = 45° and U_{10}= 20 m/s.

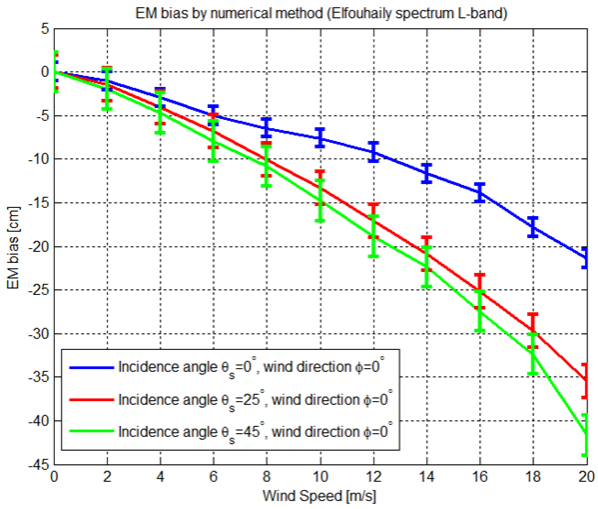

Figure 3.10 Impact of incidence angle on the EM bias using Numerical method.

In addition, the EM bias is estimated for a wind direction $\phi = 45°$, in three incidence angles $\theta_s = 0°,\ 25°, 45°$, and that is shown in Figure 3.11.

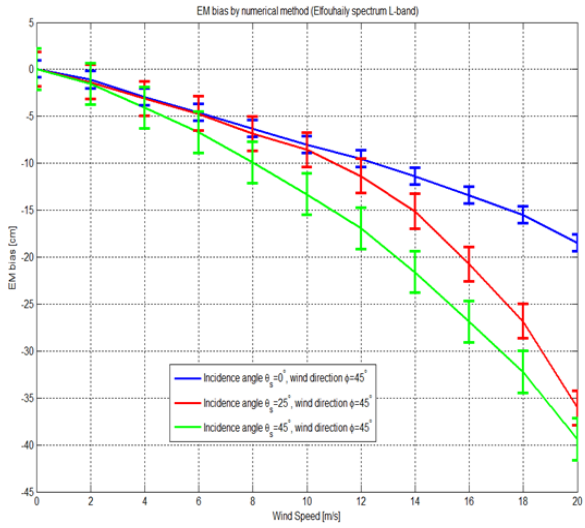

Figure 3.11 Impact of incidence angle on the EM bias using Numerical method.

By comparing the range of the estimated EM bias from both wind directions (Figure 3.10 and 3.11), it can be concluded, that the EM bias is a function of not only the incidence angle, but also the wind direction. Because of that, the impact of wind direction on the EM bias as an azimuthal impact is investigated in next section. This is an important conclusion for GNSS-R systems due to their bistatic configuration.

3.5.4- Effect of Azimuthal Angle on the EM bias

Most analytical models do not predict the dependence with the incidence angle, and only the combined model is able to predict it. However, none is able to predict the azimuthal signature that is induced by the angle between the look angle and the wind direction, the dependence on σ^0. In this section, the azimuthal dependence of the EM bias vs. the wind direction is also investigated using the basic definition (Eqn. (3.1)). Results are shown in Figure 3.12 for $\theta_{i,s} = 25°$, and for three different wind speeds 5, 10, and 15 m/s. As it can be appreciated, the EM bias dependence exhibits a non-negligible azimuthal dependence (~1.5-2 cm peak-to-peak at 10 m/s, and ~5 cm peak-to-peak at 15 m/s). The effect of the wave asymmetry is evident, and it has to be taken into account as well in the error budgets of future GNSS-R altimeters [25].

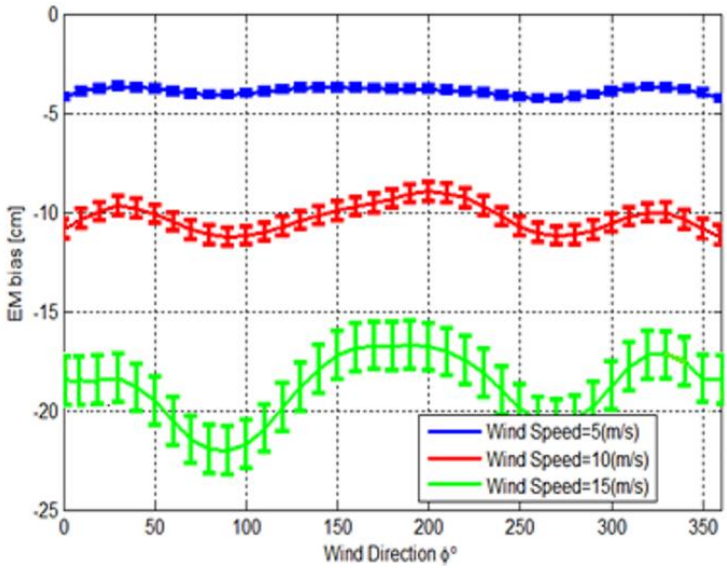

Figure 3.12 EM bias vs. wind direction using non-Gaussian sea surface and incidence angle of θ_s=25° for U_{10} = 10, 15 and 20 m/s.

3-6. Conclusions

In this chapter, Millet's EM bias combined model (WNL + MTF) has been reviewed including the effect of incidence angle. The implementation of this model has been first validated at C- and Ku-bands with existing experimental data, and then it has been extrapolated at L-band. An efficient numerical approach to compute the EM bias is proposed based on the numerical evaluation of EM bias basic definition, for a realization of the sea surface using the KA-PO scattering method. Monte Carlo simulations have been performed to reduce the uncertainty of the estimations. The proposed numerical technique has been validated against Millet's combined model, it allows to predict the dependence with frequency, incidence/scattering angle,

azimuthal angle, and wind speed, which may explain some of the differences found, since analytical models do not account for the azimuthal dependence.

The impact of the sea surface spectra used is negligible. The impact of the facet size is negligible for low wind speed conditions, but not for high wind speeds, which confirms that long waves have a stronger impact on the EM bias than the short waves, although the short ones do contribute as well.

The general trend is that the EM bias increases with decreasing frequency, increasing incidence angle, and increasing wind speed, and it exhibits an azimuthal angle modulation as well, that somehow mimics that of σ^0. At L-band, and for 12 m/s wind speed, the EM bias at nadir ($\theta_{i,s}$=0°) can be as high as 19 cm, but at large incidence angles ($\theta_{i,s}$=45°) it can increase up to 19 cm.

These values are very important and will dominate the altimetry error budget of future GNSS-R altimeters [25], unless properly corrected. The EM bias correction requires a precise knowledge of the geometry (incidence/scattering angle), and the wind speed and azimuthal angle with respect to the incidence plane, as auxiliary information.

Chapter 4 - Impact of Rain, Swell, and Surface Currents on the EM Bias in GNSS-Reflectometry

4.1- Introduction

In a chapter 3, the EM bias in a bistatic GNSS-R altimeter (L-band) was estimated for a wind-driven sea surface spectrum. In this chapter, the three-dimensional time-evolving wind-driven sea surface is also altered by rain, swell, or surface currents. As before, the generated sea surface is illuminated by a Right Hand Circular Polarization (RHCP) L-band electromagnetic wave. Then, the scattered wave is computed from each facet using the Physical Optics (PO) method. Finally, the EM bias is computed numerically under the presence of the three natural phenomena listed before. The impact of rain is a moderate decrease (in magnitude) of the EM bias due to the damping of the wind-driven waves, which is more significant as the wind speed increases. The impact of swell is a small increase (in magnitude) of the EM bias due to the change of the local incidence angles. Moreover, the impact of currents is either a moderate increase or decrease of the EM bias, depending on the sense of the current with respect to the wind.

4.2- Simulation Approach

Rain drops splashing on the sea surface create a fresh water layer (in calm conditions, under wind it gets mixed), and it induces changes in the surface roughness, that depend on the rain-rate intensity, and the drop size distribution (DSD). In this study, the log-Gaussian spectrum is used to generate the sea surface overlapped by rain-drops as it was proposed in [73], [74].

Swell is a series of mechanical propagating waves not generated by the immediate local wind, but by distant weather systems instead, where wind is blowing for a period of time over a given fetch. The swell spectrum can be modeled using a narrow-band Gaussian process by a two dimensional roughness spectrum [75], superimposed to the sea spectrum. In [75], the impact of swell on the scattering cross-section was investigated at L-band, and it was demonstrated that the scattering cross-section increased by the presence of swell over the sea surface.

Finally, sea surface currents influence the Earth's climate system, by transporting massive amounts of heat. Near-surface currents alter the sea surface roughness and can affect the scattering processes significantly. The impact over the sea surface spectrum of the sea surface currents has been accounted for using Huang's model [76].

Since the impact of these perturbing effects is small or moderate, we are only interested in the deviations with respect to the wind-driven spectrum. These models have been successfully used in the past to compute the impact of rain, swell, and currents in the sea surface emissivity at L-band [35], [36], [77].

In this chapter, the scattering cross-section of the perturbed sea surface, is computed using the PO scattering technique (e.g. [60]), and the EM bias is numerically computed (Eqn. 3.1). The computed EM bias is required to predict the performance of upcoming GNSS-R systems [25].

This chapter is organized as follows: Section 4.3 analyses the impact of rain on the EM bias, Section 4.4 the impact of swell, Section 4.5 the impact of surface currents, and finally Section 4.6 presents the conclusions.

4.3- Rain Impact on the EM Bias

Rain has significant role the heat and moisture fluxes when a raindrop falls over the water surface three type of roughness are created: craters, stalks, and crowns. The roughness degree depends on several parameters, raindrop size, and rain drop size distribution (DSD), presence of wind etc. In addition, raindrops hitting the sea surface do not change the surface roughness (through a slightly change), but also provide a fresh water layer than can affect the scattering process consequently.

The impact of rain on the scattering cross-section was investigated at Ku-band, and it was demonstrated that the scattering cross-section was dependent on the rain-rate intensity [73]. In [73], the rain spectrum was analyzed and it was proposed to have contributions from the ring-waves on the water, and from turbulence underneath the water surface. The rain-perturbed sea surface spectrum is then simulated by superimposing it to the sea spectrum and solving iteratively some conditions [74].

Finally, the rain spectrum proposed by contribution of both the ring-wave impact and the turbulence beneath the water surface. The dispersion relationship and gravity-capillary wave have been used to proposing the ring-wave spectrum. Finally, the rain spectrum formulated using the log-Gaussian wave number spectral model [73]:

$$S_k(k) = \frac{1}{2\pi} C_g S_{fp} \exp\left\{ -\pi \left[\frac{\ln\sqrt{gk + \frac{\frac{\tau}{\rho}k^3}{2\pi f_p}}}{\frac{\Delta f}{f_p}} \right]^2 \right\}, \qquad (4.1)$$

where, C_g, S_{fp}, and g are the group velocity, the power law spectral model, and the gravitational acceleration. Also f_p, Δf are the peak frequency and bandwidth respectively.

The impact of heavy rainfall is a damping of the sea waves [78]. Figure 4.1 shows the wind-driven and the rain contributions to the composite sea surface height spectrum in the highest wavenumbers.

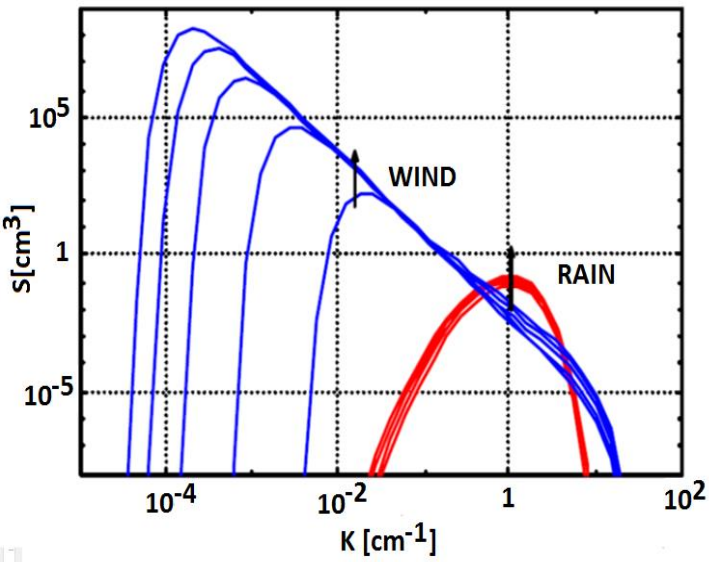

Figure 4.1 Wind-induced spectrum for wind speeds 5, 10, 15 and 20 m/s,and rain-induced spectrum for rain rates 20, 40, 60 and 80 mm/h [35].

Then, as in chapter 3 and 4, a time-dependent 6 km x 6 km size is generated in patches of 1000 m $\times$1000 m size (with $\varepsilon_r = 73 + j57.5$) as it includes the longest waves associated to the highest wind speed conditions. The incident wave illuminating the sea surface is then created: a RHCP wave at L-band (f_{L1}=1.57542 GHz), which was actually pre-recorded using a GPS data-logger. The scattered wave from a rain-perturbed sea surface is finally computed

using the PO method to obtain the scattering cross-section, as required by Eqn. 3.1.

The EM bias computed for $\theta_i = \theta_s = 25^\circ, 35^\circ$ and 45° are presented in Figure 4.2, 5.3, and 5.4, as a function of the wind speed without and with rain (R = 100 and 200 mm/h). As it can be seen, the EM bias is always smaller for rain-perturbed sea surfaces because of the damping of the large sea waves. This effect becomes more important at high wind speeds.

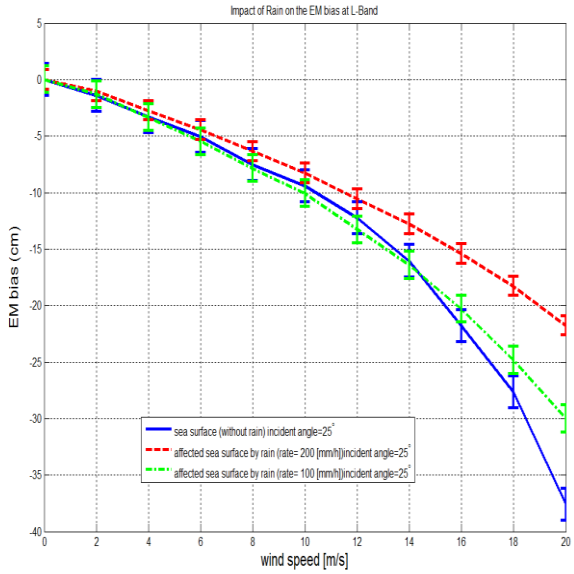

Figure 4.2 Estimated EM bias using the numerical method for the sea surfacewith and without rain (R = 100 and 200 mm/h) for incident angle $\theta_i = \theta_s = 25^\circ$.

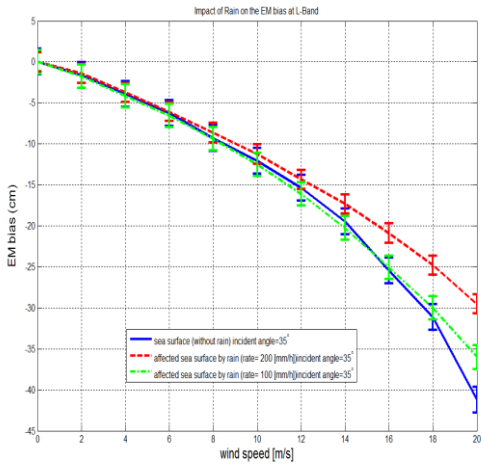

Figure 4.3 Estimated EM bias using the numerical method for the sea surfacewith and without rain (R = 100 and 200 mm/h) for incident angle $\theta_i = \theta_s = 35^{\circ}$.

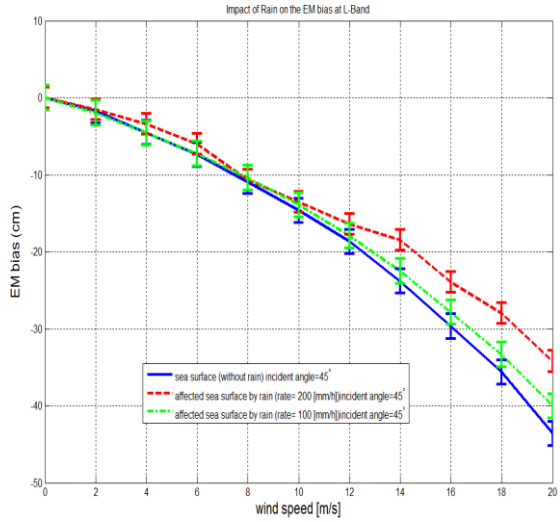

Figure 4.4 Estimated EM bias using the numerical method for the sea surface with and without rain (R = 100 and 200 mm/h) for incident angle $\theta_i = \theta_s = 45^{\circ}$.

4.4- Swell Impact on the EM Bias

The swell of impact on the scattering cross-section was investigated using the two-scale model at L, X, and Ku bands [79], [80]. It was shown that the scattering cross-section significantly affected by swell at L-band, although it was negligible at Ku-band [75].

In this study, the swell impact is modeled as a narrow-band Gaussian spectrum to the ocean spectrum proposed in [75]:

$$\Psi_{\text{swell}}(k_x, k_y) = \frac{\langle h^2 \rangle}{2\pi\sigma_x\sigma_y} \cdot \exp\left\{-\frac{1}{2}\left[\left(\frac{k_x - k_{xm}}{\sigma_x}\right)^2 + \left(\frac{k_y - k_{ym}}{\sigma_y}\right)^2\right]\right\}. \quad (4.2)$$

where $\langle h^2 \rangle$ is the height variance of the swell, σ_x and σ_y are the spectral standard deviations, and k_{xm} and k_{ym} are the spectral peak wave number of the swell in the x and y directions, respectively, which in general, are not coincident to the upwind and crosswind ones.

To illustrate this effect an $\langle h^2 \rangle = 4$ m rms height swell, with a wavelength $\Lambda_m = 400$ m ($k_m = 2\pi/\Lambda_m$), and $\sigma_x = \sigma_y = 0.0025$ m^{-1} is simulated. The computed EM bias affected by swell is shown in Figure 4.5. As it can be appreciated, the presence of swell produces an increase (in magnitude) of the EM bias. As interesting point is that, since the swell model includes very large quasi-sinusoidal waves, the impact is negligible at low wind speeds, and it is only noticeable for strong winds due to the change of the local slopes.

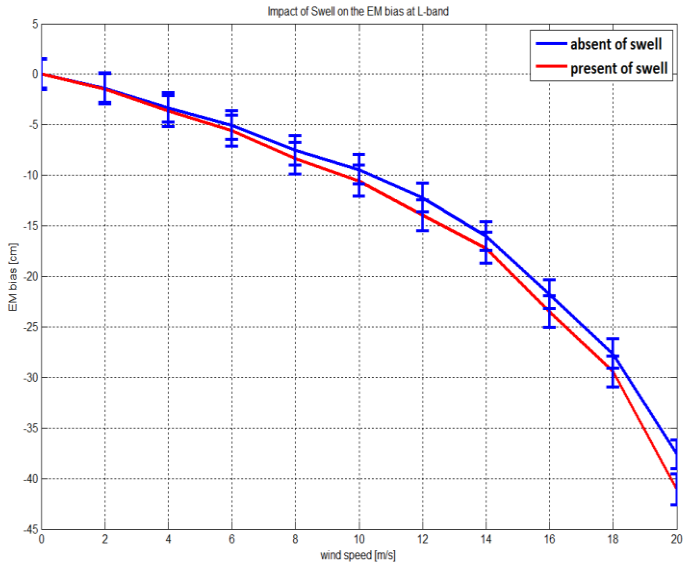

Figure 4.5 EM bias at θi=θs=25°computed with and without a swell of $\langle h^2 \rangle = 4$ m rms, $\Lambda_m = 400$ m, and $\sigma_x = \sigma_y = 0.0025$ m-1 .

4.5- Current Impact on the EM Bias

The ocean has perpetual significant impact on the human life. Usually the oceanic currents are driven by several factors: up and down motion of the tides, wind and Thermo-Haline Circulation (THC) etc.

Ocean currents affect the sea surface spectrum. When the current has the same direction and sense as the wind, the sea surface becomes less rough. On the contrary, when the current has the opposite sense (against the wind direction), the sea surface becomes rougher. In this study, the closed-form derived by Huang et al. [76] is used:

$$S(K) = \frac{a}{K^3} \cdot \frac{1}{\left(1+\frac{U_{current}}{c}\right)^7} \cdot exp\left\{-\frac{0.74 \cdot g^2}{K^2 \cdot U_{10}^4 \cdot \left(1+\frac{U_{current}}{c}\right)^4}\right\}, \qquad (4.3)$$

where K is the wavenumber, a = 4.05·10^{-3}, c is the phase velocity, U_{10} is the 10 m height wind speed, and $U_{current}$ is the current speed.

Figure 4.6, 5.7, and 5.8 show the impact of ocean currents in the EM bias as a function of the wind speed. When the current is positive (same direction as the wind), the EM bias decreases because of the reduced surface roughness, and when the current is negative (against the wind), the EM bias increases in magnitude, with a maximum increment of ~5 cm at U_{10} = 20 m/s, and $\theta_i = \theta_s = 25^{\circ}$.

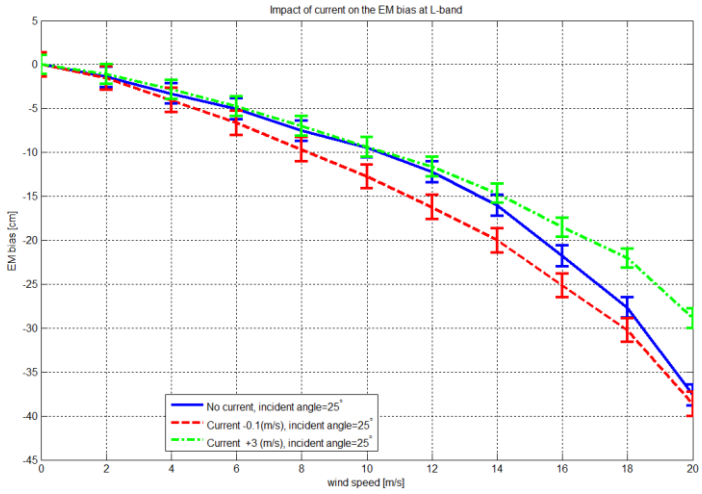

Figure 4.6 EM bias at θ_i=θ_s=25°, computed without currents, and with currents with $U_{current}$ = +3 m/s and $U_{current}$ = -0.1 m/s.

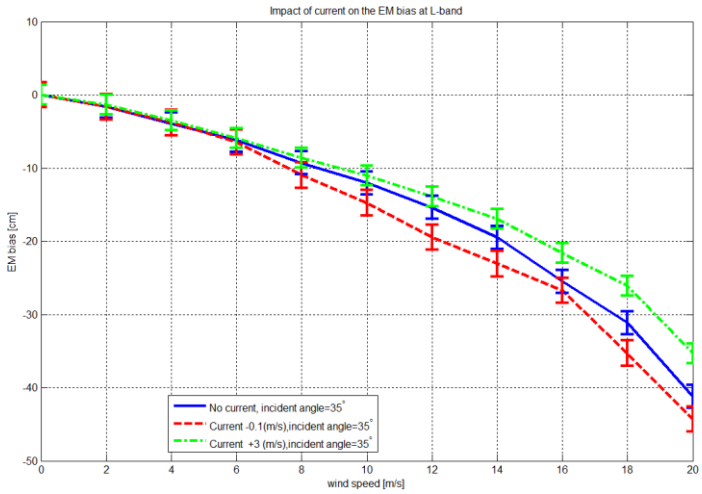

Figure 4.7 EM bias at $\theta_i=\theta_s=35°$, computed without currents, and with currents with $U_{current}$ = +3 m/s and $U_{current}$ = -0.1 m/s.

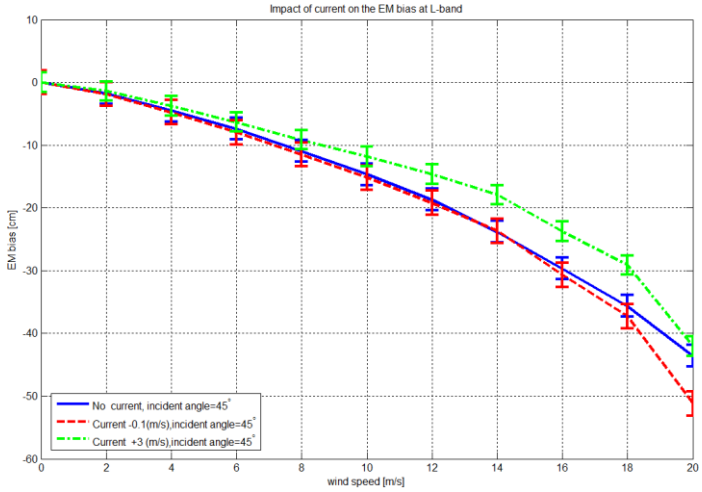

Figure 4.8 EM bias at $\theta_i=\theta_s=45°$, computed without currents, and with currents with $U_{current}$ = +3 m/s and $U_{current}$ = -0.1 m/s.

Figure 4.6, 5.7, and 5.8 show, the presence of the ocean current with opposite of wind direction is increased the EM bias as expected (because of roughness increment). It should be mentioned that by presence of ocean current, the EM bias begins to increase from low wind speed to higher wind speeds.

4.6- Conclusions

The EM bias dependence on the wind speed and the incidence angle was studied in [51], [52], [81]. The impacts on the EM bias of other natural phenomena influencing the sea surface roughness have been studied in this work for a bistatic configuration at L-band (GNSS-R system). The presence of heavy rainfall over the sea surface affects the EM bias, but this effect is only detectable at high wind speeds, and for large rain rates. At $\theta_i = \theta_s = 25^\circ$, the EM bias decreases (in magnitude) by ~5 cm for U_{10} = 20 m/s and R = 200 mm/h.

The impact of swell over the ocean surface is an increase of the EM bias values, although this effect is weak, and only noticeable (~2-3 cm) for high wind speeds (U_{10} = 20 m/s) and large swells ($\langle h^2 \rangle = 4$ m rms height).

Finally, the effect of surface currents can be either an increase or a decrease of the EM bias, depending if the current is against the wind or if it has the same direction and sense. EM bias largest increase occurs at moderate wind speeds (U_{10} = 15 m/s) while incident angle is $\theta_i = \theta_s = 25^\circ$, and it can be up to ~8 cm for surface currents of $U_{current}$ = -3 m/s. However, at higher incident angle ($\theta_i = \theta_s = 45^\circ$), presence of current is increased the EM bias after moderate wind speed (U_{10} = 12 m/s).

Since these natural effects produce a non-negligible variability of the EM bias (~50 % change), it is important to account for them in order to make a good estimate of this residual error.

Chapter 5 - Time-Domain Statistics of the Electromagnetic Bias in GNSS-Reflectometry

5.1- Introduction

The time-domain statistics of the EM bias in GNSS-Reflectometry (GNSS-R) are investigated in this chapter. A three-dimensional time-evolving sea surface is generated using Elfouhaily's ocean surface height spectrum and spreading function. This surface is illuminated by a RHCP electromagnetic wave at L-band. Then, the scattered waves are computed using the Physical Optics method under the Kirchhoff Approximation. The electro-magnetic (EM) bias is estimated using a numerical technique previously validated at C- and Ku-bands, and then extrapolated at L-band. Monte Carlo simulations for different sea surface realizations consecutive in time are performed so as to analyze the EM bias statistics (up to 4^{th} order moments). Histograms and distribution of the time domain EM bias also are used for statistical interpretation. All statistical descriptors confirmed the EM bias has a non-Gaussian behavior. This study is important to assess the optimum processing of the coherently integrated waveforms, and to assess the residual EM bias in future GNSS-R altimetry missions.

5.2- Simulation Approach

The term Global Navigation Satellite System Reflectometry (GNSS-R) encompasses various remote sensing techniques. GNSS-R exploits the navigation satellite EM waves scattered from points on the Earth's surface (water, ice, or land surfaces), to derive geophysical properties. Depending on the antenna directivity and–eventually the number of beams, and receiver characteristics, several reflected waves can be used simultaneously to perform

scatterometry and/or altimetry observations from different directions. Recently, the EM bias was numerically computed for bi-dimensional bistatic GNSS-R altimeters using the Geometric Optics method [51], and then improved using the Physical Optics method [52]. This model was validated against the combined model [13], [14], and then extended to L-band. An angular dependence with the incidence/scattering and azimuth angles was found, in addition to the wind speed dependence.

In this study, the sea surface is generated using Elfouhaily's spectrum and spreading function [50], because of its capability to generate the full wave spectra (long and short waves). It is well known that the ocean surface is not Gaussian, as confirmed in [52], following the procedure described in [58].

In this work, the numerical method in [52] using the Physical Optics (PO) method under the Kirchhoff Approximation (KA) is applied to estimate the time-domain evolution of the EM bias, and to compute its statistics.

This document is organized as follows: Section 5.3 summarizes the steps required to compute the off-nadir EM bias, using the numerical method described in [52], Section 5.4 presents the statistical study on the time-domain EM bias, and Section 5.5 presents the conclusions.

5.3- Statistical Study on the Time-Domain EM Bias

In this section, the EM bias is computed in the time-domain using the numerical method described above. The estimation of the EM bias in the time-domain requires the generation of the sea surface height in the time-domain explained above. Actually, the estimation of the EM bias as a function of time, even in steps of 1 s, significantly increases the computational cost. The

variation of the instantaneous sea surface height (ξ) affects the scattering process, and therefore the radar cross-section density (σ^0), the two variables from which the β_{EM} depends.

Here, the histograms of the time-domain EM bias are computed, as well as the first (mean), second (variance), third (skewness), and fourth (kurtosis) moments.

5.4- Results

The estimated EM bias time series is presented in Figure 5.1 for an incidence/scattering angle of 25° (nadir looking, monostatic case), 35°, and 45°, and a wind direction of 45° vs. the look direction, as a function of the wind speed. Other scenarios have been tested, including different time step (1 s), but results are nearly indistinguishable. Error bars show the 95% confidence limits estimated from 10 Monte Carlo realizations.

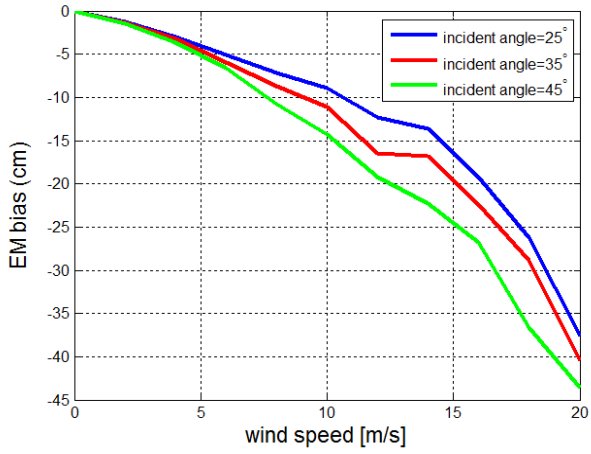

Figure 5.1 Estimated EM bias for θ_i=θ_s=25°,35°,45° and φ=45°.

If the wind speed is set as a constant, but the sea waves evolve with time in time steps of 50 ms, the time-domain evolution of the EM bias can be computed[6]. Results are presented in Figure 5.2 for $\theta_i = \theta_s = 25°$, and for three wind speeds: 5, 10, and 15 m/s. As it can be appreciated, increasing the wind speed not only increases (in absolute value) the average EM bias, but its variance as well, as shown in Table 5.1.

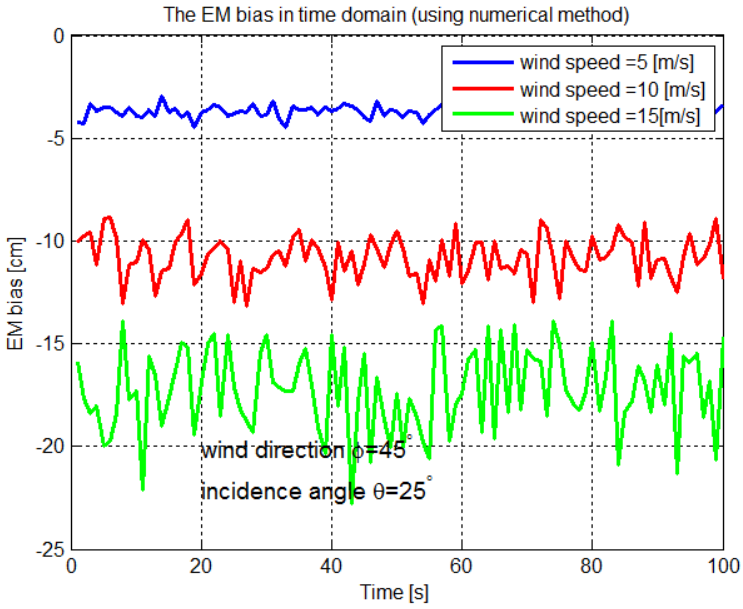

Figure 5.2 Computed time-evolution of the EM bias for U_{10} = 5, 10, and 15 m/s, incidence angle $\theta_i=\theta_s=25°$, and wind direction $\varphi=45°$.

[6] Typical configuration of GNSS-R scatterometer, such as UK TDS-1 or the upcoming NASA CYGNSS mission, are 1 ms coherent integration, followed by 1000 incoherent averaging (total = 1 s). GNSS-R altimeters require a much shorter incoherent averaging, 10-50 ms, followed by retracking of the waveform, and subsequent incoherent averaging, in order not to degrade the altimetry performance.

Figure 5.2 shows another interesting feature, although the fluctuations of the EM bias are quite noisy, it is evident that the higher the wind speed, the faster the fluctuations are, as it can be noticed in Figure 5.3, which is probably due to the fast changes in the small scales, and not on the long waves, which travel at a much slower speed.

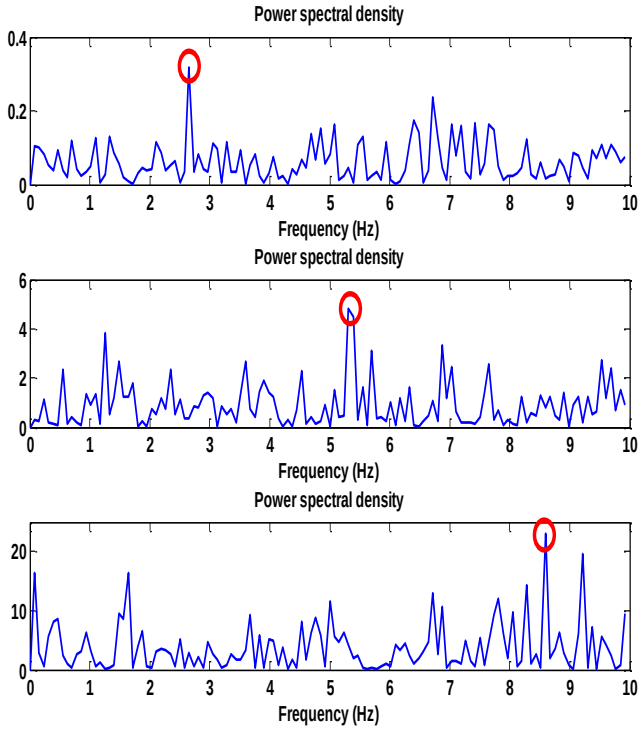

Figure 5.3 Power spectral density of the EM bias fluctuation (mean removed) for $\theta_i=\theta_s=25°$, $\varphi=45°$. U_{10} = 5 m/s (top), 10 m/s (center), and 15 m/s (bottom).

Figure 5.4 shows the histograms of the EM bias time series for the three different wind speeds studied. As it can be appreciated, for increasing wind speeds, the histograms tend to be less Gaussian. The Skewness and Kurtosis

parameters in Table 5.1, 5.2,and 5.3 show that with increasing wind speeds, the EM bias histogram become more asymmetrical, and the Kurtosis also decreases, departing from 3, which indicates a more rounded peak around the mean, and a departure from being Gaussian [82]. The obtained histograms demonstrate that the EM biases have a non-Gaussian PDF.

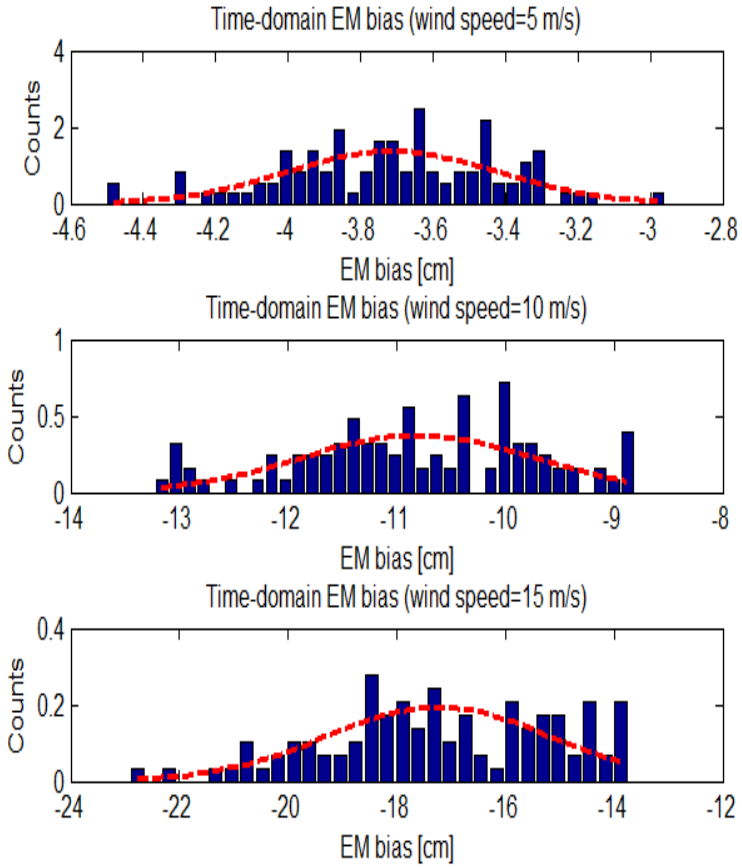

Figure 5.4 Histograms of the EM bias time series for $\theta_i=\theta_s=25°$, $\varphi=45°$, and U_{10} = 5 m/s (top), 10 m/s (center), and 15 m/s (bottom).

Table 5.1 EM bias time series main statistical descriptors for $\theta_i=\theta_s=25°$, $\varphi=45°$, and U_{10} = 5 m/s (top), 10 m/s (center), and 15 m/s (bottom).

U_{10}	$\langle\beta_{EM}\rangle$ [cm]	$\sigma_{\beta_{EM}}$ [cm]	$S_{\beta_{EM}}$ (unitless)	$K_{\beta_{EM}}$(unitless)
5 m/s	-3.72	0.292	-0.475	5.44
10 m/s	-9.73	0.959	-0.493	5.03
15m/s	-17.2	2.06	-0.592	4.84

Table 5.2 EM bias time series main statistical descriptors for $\theta_i=\theta_s=35°$, $\varphi=45°$, and U_{10} = 5 m/s (top), 10 m/s (center), and 15 m/s (bottom).

U_{10}	$\langle\beta_{EM}\rangle$ [cm]	$\sigma_{\beta_{EM}}$ [cm]	$S_{\beta_{EM}}$ (unitless)	$K_{\beta_{EM}}$(unitless)
5 m/s	-4.12	0.239	-0.675	5.75
10 m/s	-12.3	0.911	-0.871	4.52
15m/s	-20.3	1.59	-0.896	4.29

Table 5.3 EM bias time series main statistical descriptors for $\theta_i=\theta_s=45°$, $\varphi=45°$, and U_{10} = 5 m/s (top), 10 m/s (center), and 15 m/s (bottom).

U_{10}	$\langle\beta_{EM}\rangle$ [cm]	$\sigma_{\beta_{EM}}$ [cm]	$S_{\beta_{EM}}$ (unitless)	$K_{\beta_{EM}}$(unitless)
5 m/s	-4.96	0.176	-1.041	6.95
10 m/s	-13.8	0.691	-1.351	4.59
15m/s	-24.1	1.28	-1.516	4.42

By comparing Table 5.1, 5.2, and 5.3, the impact of the incidence angle on the EM bias in the time-domain clearly is shown in the mean and the standard deviation. In addition, the time-domain EM bias non-Gaussian behavior is verified using third and fourth moment descriptors.

5.5- Conclusions

In this chapter, the time domain statistics of the EM bias have been computed using a numerical simulator that allows: 1) to mimic the RHCP transmitted wave by the GPS Space Vehicles, that impinges the time-evolving surface of the sea, 2) to compute the scattered fields, and 3) to estimate the EM bias for each set of parameters (wind speed, incidence/azimuth angles).

By computing the time series of the EM bias under different wind speed conditions, it is found that not only the average value depends on the wind speed, but also the variance, the Skewness, and Kurtosis. As the wind speed increases, the EM bias histograms depart from a Gaussian distribution and the variance increases, which translate into a larger uncertainty of the EM bias itself during the incoherent integration time. In addition, since the EM bias does not follow a Gaussian distribution, it does not average as $\sqrt{N}$, being N the number of measurements during the whole integration time (e.g. N=1000 in 1 s, if the coherent integration time is 1 ms). These values are very important in the estimation of the residual EM bias for GNSS-R altimetry error budgets [25].

Chapter 6 - Future Research Prospective

The present thesis has worked on three main topics: GNSS systems, ocean scattering models, and the ocean spectra. GNSS transmitter is continuously broadcasting RHCP at L-band towards the Earth, which are then reflected back a LHCP (majority) and RHCP (minority).

Most GNSS receivers work with just one L-band antenna, but in this work an L-band antenna array has simulated to collect the scattering waves.

Both GO and PO scattering methods have been simulated in this thesis and the PO superiority is demonstrated in final EM bias computation scales. In fact, LHCP just scattered waves are used to compute the EM bias. In the future work the RHCP components can also be involved. By current experience, Method of Moment (MoM) scattering model is suggested to simulate the scattering waves for the future work, because it is more accurate than both previous scattering methods. It should be noted that this method (MoM) needs much modern computer facilities. In addition, improved scattering methods can be used to account for multipath scattering effects.

In the present Ph.D. thesis, three well-known ocean surface spectra have been considered and simulated because of their ability to produce non-Gaussian surface roughness. The ocean surface new spectrum can be used in the future studies to simulate the sea surface (if it can produce non-Gaussian roughness surfaces).

Appendix A. Electromagnetic Scattering Models

Based on the electromagnetic point of view there are several techniques to estimate the scattering, as mentioned following; 1- GO, 2- PO, 3-Modal Technique (MT), 4- Integral Equation, 5- Geometrical Theory of Diffraction (GTD), 6- Physical Theory of Diffraction (PTD), each of them has its advantages and drawbacks. In this part, several applicable scattering techniques, which are proper for roughness will be presented GO, and PO. Based on the application and frequency, the scattering method will be selected for problem. In this thesis, to investigate the sea surface scattering, both GO and PO scattering techniques are applied and discussed.

The polarization of the scattered wave is the radiated wave describing the time-varying direction and relative magnitude of the electric field vector. The circular polarization wave is considered in this work, which is the combination two linear components. When the electric field vector rotates in a circular direction in space at clockwise direction, which is called right hand circular polarization. The basic RHCP wave relation is written as [59]:

$$E = E_R\{[\hat{a}_X - j\hat{a}_Y]\, e^{-j(\omega t - kz)}\}, \qquad (A.1)$$

where E_R is amplitude, $\hat{a}_X, \hat{a}_Y$ are horizontal and vertical axis, ω is angular frequency, t is time, k is wave number, z the traveled distance in the $\hat{z}$ axis.

A.1- Scattering cross-section definition

The propagated wave from scattered wave from the surface can be described with remarkable accuracy using Maxwell's equations and auxiliary relationship. Maxwell equations are applied to compute the electrical and magnetic field, which is reflected from scatterer surfaces. The spatial distribution of the scattered wave is so-called instead the terms of scattering

cross-section or radar cross-section. The basic definition of radar cross-section (σ) is written as [83]:

$$\sigma = 4\pi R^2 \frac{|E_s|^2}{|E_i|^2}, \qquad (A.2)$$

where, R is the travel path distance, E_i , E_s are the electrical incidence and scattered wave respectively. The normalized scattering cross-section is defined as (σ^0), which will be applied in the next sections. The scattering coefficient is so called as ‘‘sigma-naught’’ (σ^0) and given as [83]:

$$\sigma^0 = \langle \frac{\sigma_i}{A_i} \rangle, \qquad (A.3)$$

where, σ_i is the radar cross-section of each facet, A_i is the area associated to scatter the wave.

A.2- Kirchhoff approach under the geometric optics approximation GO scattering models

In order to perform a study as realistic as possible, a true direct (multipath-free) GPS signal was recorded. This signal is used to simulate the signal illuminating a synthetic sea surface. The scattered wave is then computed using the Physical Optics (PO) method under the Kirchhoff approximation (KA) because of its higher accuracy [60].

The GO is an approximate high frequency method for defining wave propagation for incident, reflected, and refracted waves. Originally, this method was developed to analyze the scattering of wave at adequate high frequencies. In fact, it uses the ray concept to justification. The scattering for high frequency depends on both phenomena, geometry of scatterer object, and incidence wave. It follows the Snell’s law in reflection.

Here, the RHCP wave is illuminating over the generated sea surface, the incidence wave. The sea surface as a reflector will change the scattered wave polarization, amplitude, and phase; in addition, the sea surface has its complex permittivity. The incidence wave is applied from [84]:

$$\bar{E}_{i_k} = \left(E_{v_{ik}}\widehat{v_{\iota k}} + E_{h_{ik}}\widehat{h_{\iota_k}}\right)e^{-j\overline{k_{\iota k}}\cdot\bar{r}}, \qquad (A.4)$$

where the $\widehat{v_{\iota k}}$ is the vertical normal vector of incident wave, and $\widehat{h_{\iota_k}}$ is the horizontal normal vector of incident wave. The definition these bias vectors are:

$$\widehat{v_{\iota k}} = \widehat{h_{\iota k}} \times \widehat{k_{\iota k}}, \qquad (A.5)$$

$$\widehat{h_{\iota k}} = \frac{\widehat{h_{\iota k}} \times \hat{z}}{\left|\widehat{h_{\iota k}} \times \hat{z}\right|}, \qquad (A.6)$$

Moreover, the electrical scattered wave from each facet has computed with relation:

$$\bar{E}_{s_k} = \left(E_{v_{sk}}\widehat{v_s} + E_{h_{sk}}\widehat{h_s}\right)e^{-j\overline{k_s}\cdot\bar{r}}, \qquad (A.7)$$

where, $\widehat{k_s}$ is the direction of scattered wave, the $\widehat{v_s}$ is vertical bias of scattered wave and the $\widehat{h_s}$ is horizontal bias of scattered wave. Here, we should emphasis again that, the electrical scattered wave of each facet has decomposed into two components, where $E_{h_{sk}}$the electrical horizontal is scattered wave and $E_{v_{sk}}$ is the electrical vertical scattered wave.

The scattered wave is related to incident wave based on the scattering function matrix:

$$\begin{bmatrix} E_{vsk} \\ E_{hsk} \end{bmatrix} = e^{-j\overline{k_s}\cdot\bar{r}}\,\bar{\bar{f}}\begin{bmatrix} E_{vik} \\ E_{hik} \end{bmatrix}, \qquad (A.8)$$

$$\widehat{v_s} = \widehat{h_s} \times \widehat{k_s}, \qquad (A.9)$$

$$\widehat{h_s} = \frac{\widehat{h_s} \times \hat{z}}{\left|\widehat{h_s} \times \hat{z}\right|}, \qquad (A.10)$$

The scattering coefficient matrix are calculated with the help of Fresnel reflectivity relation for each facet and its result is illustrated in Figure A.2 [84]:

$$\bar{\bar{f}} = \begin{bmatrix} f_{vvk} & f_{vhk} \\ f_{vhk} & f_{hhk} \end{bmatrix}, \qquad (A.10)$$

$$f_{vvk} = (\hat{v}_{ik}.\hat{p}_{ik})R_v(\theta_{lk})(\hat{v}_s.\hat{p}_{sk}) + (\hat{v}_{ik}.q_k)R_h(\theta_{lk})(\hat{v}_s.\hat{q}_k), \qquad (A.11)$$

$$f_{vhk} = (\hat{h}_{ik}.\hat{p}_{ik})R_v(\theta_{lk})(\hat{v}_s.\hat{p}_{sk}) + (\hat{h}_{ik}.\hat{p}_{ik})R_h(\theta_{lk})(\hat{v}_s.\hat{q}_k), \qquad (A.12)$$

$$f_{hvk} = (\hat{v}_{ik}.\hat{p}_{ik})R_v(\theta_{lk})(\hat{v}_s.\hat{p}_{sk}) + (\hat{v}_{ik}.q_k)R_h(\theta_{lk})(\hat{h}_s.\hat{q}_k), \qquad (A.13)$$

$$f_{vhk} = (\hat{h}_{ik}.\hat{p}_{ik})R_v(\theta_{lk})(\hat{v}_s.\hat{p}_{sk}) + (\hat{h}_{ik}.\hat{q}_k)R_h(\theta_{lk})(\hat{h}_s.\hat{q}_k), \qquad (A.14)$$

where, f_{vvk} is reflection coefficient of vertical component incident wave and vertical component scattered wave, and f_{vhk} is reflection coefficient of vertical component incident wave and horizontal component scattered wave, f_{hhk} is reflection coefficient of horizontal component incident wave and horizontal component scattered wave, and f_{hvk} is reflection coefficient of horizontal component incident wave and vertical component scattered wave. Also in continue, the Fresnel reflectivity equations have been expressing between the local Fresnel coefficient R_v, R_h for different polarization modes of incident and reflected waves, and $\Re$ has shown the polarization-dependent reflection coefficient [59]:

$$R_v(\theta_{lk}) = \frac{\eta_1 cos\theta_{lk} - \eta_2\sqrt{1 - \left(\frac{k_1}{k_2}\right) sin^2\theta_k}}{\eta_1 cos\theta_{lk} + \eta_2\sqrt{1 - \left(\frac{k_1}{k_2}\right) sin^2\theta_k}}, \qquad (A.15)$$

$$R_h(\theta_{lk}) = \frac{\eta_2 cos\theta_{lk} - \eta_2\sqrt{1-\left(\frac{k_1}{k_2}\right)sin^2\theta_k}}{\eta_2 cos\theta_{lk} + \eta_2\sqrt{1-\left(\frac{k_1}{k_2}\right)sin^2\theta_k}}\ , \qquad (A.16)$$

where η_1 and η_2 are the intrinsic impedance and k_1 and k_2 wave numbers of scattered wave medium and sea surface, and also $\theta_{lk} = \cos^{-1}(\widehat{n_k}.\widehat{k_s})$ is the angle between facet normal vector and receiver looking direction.

By having the reflectivity's relation between linear components, the interrelations for all combination has been calculated [29]:

$$\Re_{RR} = \Re_{LL} = \frac{1}{2}(R_{VV} + R_{HH}), \qquad (A.17)$$

$$\Re_{RL} = \Re_{LR} = \frac{1}{2}(R_{VV} - R_{HH}), \qquad (A.18)$$

$$\Re_{VV} = \frac{\varepsilon sin\theta - \sqrt{\varepsilon - cos^2\theta}}{\varepsilon sin\theta + \sqrt{\varepsilon - cos^2\theta}}, \qquad (A.19)$$

$$\Re_{HH} = \frac{sin\theta - \sqrt{\varepsilon - cos^2\theta}}{sin\theta + \sqrt{\varepsilon - cos^2\theta}}\ , \qquad (A.20)$$

where, the subscripts are stand for different polarization modes, R, L, V, and H, for right hand circular, left hand circular, vertical and horizontal leaner polarization. The facet unit vectors are given [85]:

$$\widehat{q_k} = \frac{\widehat{k_s}\times\widehat{n_k}}{|\widehat{k_s}\times\widehat{n_k}|} = \frac{\widehat{k_\iota}\times\widehat{n_k}}{|\widehat{k_\iota}\times\widehat{n_k}|}\ , \qquad (A.21)$$

$$\widehat{p_{\iota k}} = \widehat{q_k} \times \widehat{k_{\iota k}}\ , \qquad (A.22)$$

$$\widehat{p_{sk}} = \widehat{q_k} \times \widehat{k_s}\ , \qquad (A.23)$$

where, $\widehat{n_k}$ is the normal vector, and $\widehat{p_{ik}}$ and $\widehat{p_{sk}}$ are orthonormal vectors. By considering the geometrical positions of transmitter and receiver in the remote sensing application, we should choose an appropriate coordinate system (see Figure A.1).

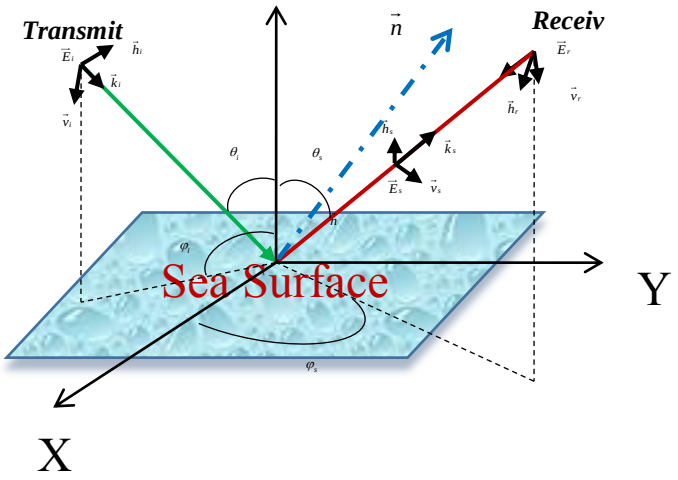

Figure A.1 The configuration a complete procedure for incident and scattered and the ocean surface.

The spherical coordinate of transmitter and receiver system parameters are given [85]:

$$\hat{k}_i = sin\theta_i cos\varphi_i \hat{x} + sin\theta_i cos\varphi_i \hat{y} + cos\theta_i \hat{z}\,, \qquad (A.24)$$

$$\hat{v}_i = cos\theta_i cos\varphi_i \hat{x} + cos\theta_i sin\varphi_i \hat{y} - sin\theta_i \hat{z}\,, \qquad (A.25)$$

$$\hat{h}_i = -sin\varphi_i \hat{x} + cos\varphi_i \hat{y}\,, \qquad (A.26)$$

$$\hat{k}_s = sin\theta_s cos\varphi_s \hat{x} + sin\theta_s cos\varphi_s \hat{y} + cos\theta_s \hat{z}\,, \qquad (A.27)$$

$$\hat{v}_s = cos\theta_s cos\varphi_s \hat{x} + cos\theta_s sin\varphi_s \hat{y} - sin\theta_s \hat{z}\,, \qquad (A.28)$$

$$\hat{h}_s = -sin\varphi_s \hat{x} + cos\varphi_s \hat{y}\,, \qquad (A.29)$$

where, $\widehat{v_i}$ and $\widehat{h_i}$ are vertical and horizontal components of the incident wave, and $\widehat{v_s}$ and $\widehat{h_s}$ are vertical and horizontal components of the scattered wave, and also θ_i and φ_i are azimuth and elevation angles of transmitter position, θ_s and φ_s are azimuth and elevation angles of receiver position. The sea surface scattering coefficient of scattering matrix is computed and presented in Figure A.2.

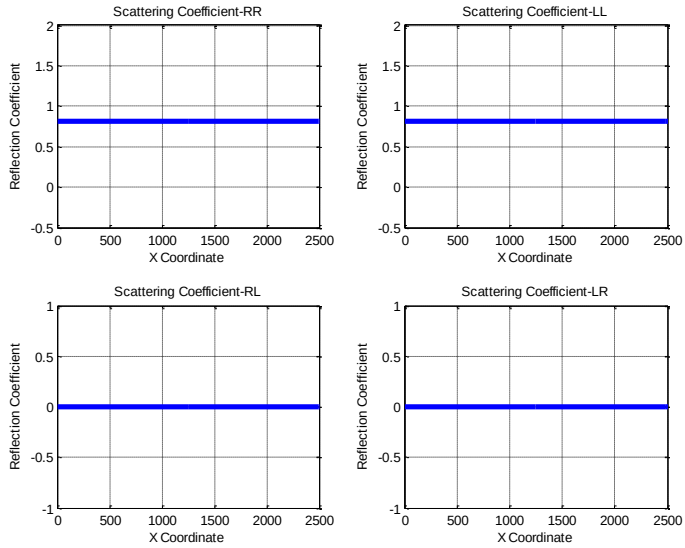

Figure A.2 Reflection Coefficient matrix of the Sea surface, (a), Reflection Coefficient Scattering Matrix from the smooth sea surface, (b), Reflection Coefficient Scattering Matrix from the windy sea surface (wind speed 10 m/s).

The sea surface scattering from over receiver viewpoint using GO method is computed (Fresnel zone effect) and illustrated in Figure A.3.

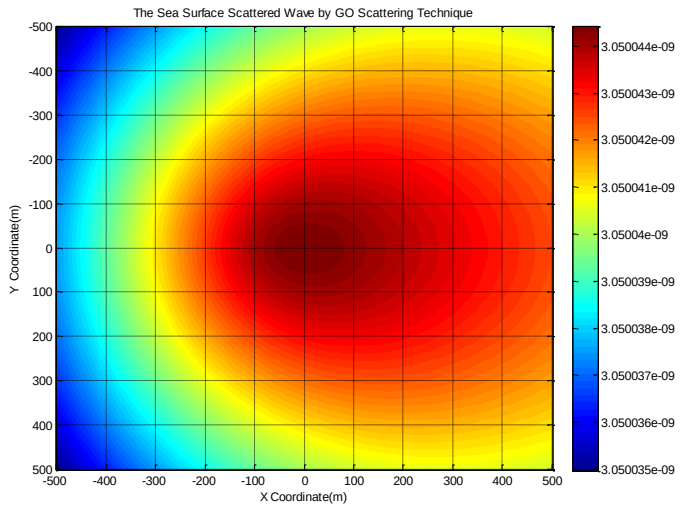

Figure A.3 The Fresnel effect of scattered from the sea surface (obtained by GO).

In this part, using the recorded GPS wave the surface illuminated (using bi-static scenario) and the impact of incidence angle on the scattering cross-section investigated, that is illustrated in Figure A.4. In addition, the impact of azimuthal angles over the scattering cross-section is considered Figure A.5.

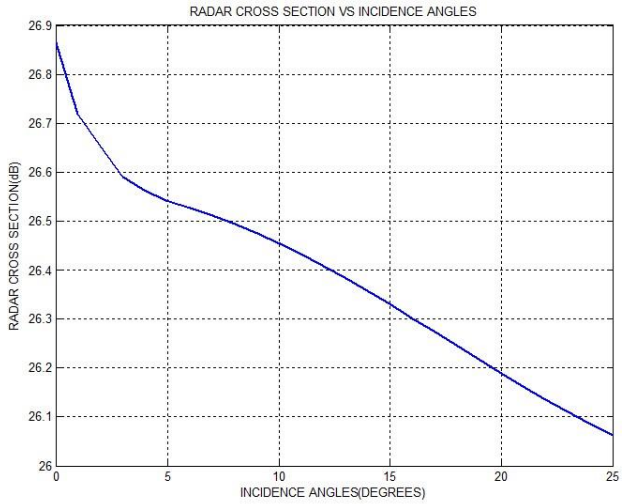

Figure A.4 Impact of incidence angle on the scattering cross-section.

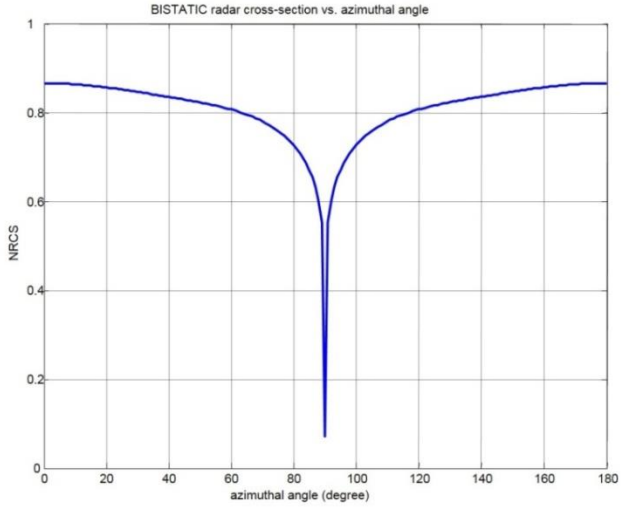

Figure A.5 Impact of azimuthal angles on the scattering cross-section.

Moreover, by synthetic sea surface impact of frequency over the scattering cross-section is computed using GO method and it is presented in Figure A.6.

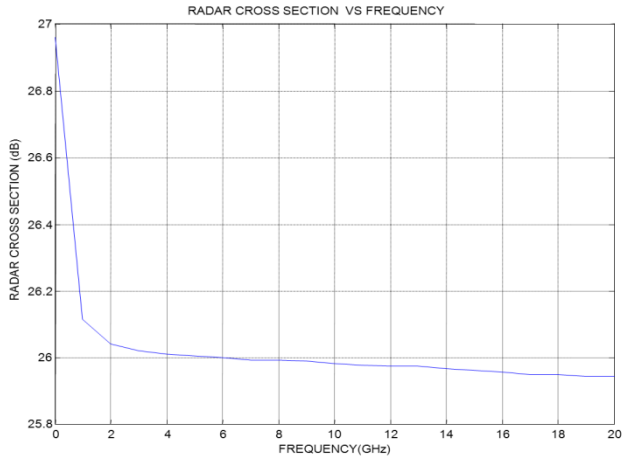

Figure A.6 Frequency mpact on the scattering cross-section using GO method.

As it seen, by increasing the frequency, the magnitude of scattering cross-section is reduced as expected. Impact of azimuthal variation over the scattering also is estimated and illustrated in Figure A.7.

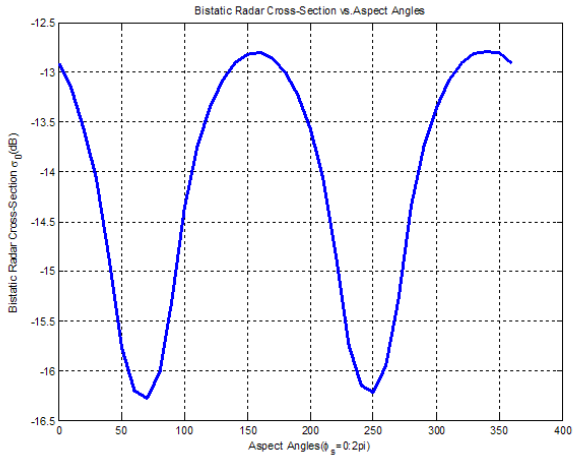

Figure A.7 Impact of azimuthal angle on the scattering cross-section using GO method.

A.3- The Kirchhoff Method under Physical Optics Approximation

First, from the conception that a circular polarized wave is a basic combination of two orthogonal linear polarized waves, i.e. H-pol and V-pol [59]:

$$E_{RHCP} = \left(\overrightarrow{E_V} \pm j\overrightarrow{E_H}\right)\exp(-j\mathbf{k}\mathrm{r}), \qquad (A.26)$$

The sea surface scattered field can be found using the Kirchhoff Approximation Physical Optics (KA-PO) method. The induced current on the sea surface is:

$$\overrightarrow{J_s} = 2\hat{n} \times \hat{H}, \qquad (A.27)$$

where $\hat{n}$, $\hat{H}$ are the normal vector, and the magnetic field vector of the incidence wave, and $\mathbf{k} = k.\hat{k}$ (k is the wave number and its direction vector). Then, the scattering over a finite metallic rectangular plate size $(a \times b)$ is [59]:

$$E_r^s \cong 0, \tag{A.28}$$

$$E_\theta^s = C\frac{e^{-jkr}}{r}\left\{\cos\theta_s \sin\phi_s \left[\frac{\sin(X)}{X}\right]\left[\frac{\sin(Y)}{Y}\right]\right\}, \tag{A.29}$$

$$E_\varphi^s = C\frac{e^{-jkr}}{r}\left\{\cos\theta_s \left[\frac{\sin(X)}{X}\right]\left[\frac{\sin(Y)}{Y}\right]\right\}, \tag{A.30}$$

$$X = \frac{ka}{2} sin\theta_s cos\varphi_s, \tag{A.31}$$

$$Y = \frac{kb}{2}(sin\theta_s cos\varphi_s - sin\theta_i), \tag{A.32}$$

$$C = -j\eta\frac{abkH_0}{2\pi}, \tag{A.33}$$

where H_0 is the magnitude of the incident magnetic field, and η is the intrinsic impedance, θ_s and φ_s are scattered field elevation and azimuth angles. In the case of a non-metallic surface, the scattered field can be computed using the Impedance Boundary Condition (IBC) as in Eqns. A.26-A.33, multiplying Eqns. A.29 and A.30 by the Fresnel reflection coefficients [71]. Finally, a 5×5 microstrip patch array with $\frac{\lambda}{2}$ element spacing is used to simulate the receiving antenna.

A.4- Kirchhoff Approximation

In the tangent plane or Kirchhoff approximation, the Green's vector theorem has been applied to compute the scattered wave from rough surface, which is proposed and modified in, that is given [83]:

$$E^s = K\hat{n}_s \times \int [\hat{n} \times E - \eta_s \hat{n}_s \times (\hat{n} \times H)]\, e^{jk_s r.\hat{n}_s} dS\,, \tag{A.34}$$

$$K = -\frac{jk_s e^{-jk_s R_s}}{4\pi R_0}. \tag{A.35}$$

where, $\hat{n}_s$ is unit vector in the scattered direction, $\hat{n}$ is unit vector normal of surface, and η_s, k_s are the intrinsic impedance and wave number of the

scattering surface. R_0 is distance from the center of surface to the receiver, E, H are the electric and magnetic fields on the interface. Two basic assumptions, the tangential plane approximation "the total fields at a point on the surface is equal to incident field plus the reflected one'', and stationary-phase approximation "it means that the scattering will occur only the specular direction" have been used for describing the roughness surface scattering fields.

Thus, the statistical surfaces are considered, their horizontal scale roughness (as the correlation length), must be larger than the incident wavelength and their vertical-scale roughness (as the standard deviation of surface heights), and must be small sufficient, so that the average radius of curvature is larger than the incident wavelength [83].

Appendix B. Hardware Reports

B.1- Recording the direct GPS signal

In this thesis, to making the situation more realistic, the GNSS signal is recorded using GNSS reviver, low noise amplifier (LNA) amplifier and L band ceramic patch L-band (RHCP) antenna. The LNA amplifier and ceramic antenna has made in RS-LAB and both performances have checked prior record.

B.2- Amplifier and GPS Antenna

A low noise amplifier (LNA) has applied based on the general receiver block diagram. Certainly, the amplifier will amplify both signal and noise simultaneously, so we should not have expectation to achieve better signal to noise ratio, practically. However, in the designing step, our goal is that the amplifier should be designed how to minimize the noise level and increase the main signal level. In experimental part, a microwave LNA is utilized. The LNA specification has been tested (based on L band frequency) by contribution of a vector network analyzer (ROHDE & SCHWRTZ-ZVB) and the S-parameters have obtained. A picture from recording process has taken and illustrated in Figure B.1.

Figure B.1 Recording direct GPS signal process using GPS patch ceramic Antenna and Microwave amplifier (LNA), receiver and relevant equipments.

RHCP antenna at L-band mounted over a non-metallic bar is used (because of noise) to recording the direct signal. To avoid of interference of reflected GPS signals, record process is done from height more than 15 meters.

B.3- Validating Visible GPS Satellites

Among several GPSs satellites, just some of them are visible in over the Barcelona, Spain on 5 Oct 2013. As it has been mentioned, the software module can indicate the visible satellites to indicate the GNSS receiver position. The software performance is captured during monitoring visible satellites.

Appendix C. Generating a Non-linear the Sea Surface

Modeling the sea surface with realism conditions is impossible but several efforts have been performed. The hydrodynamic description of the sea surface and its interaction with the wind is an extra complex problem. To make progress towards a realistic useful model, some simplifying hypotheses have been used into the proposed ocean spectra.

As it known that, the ocean waves are produced by the wind, the stronger wind is able to generate longer waves. The natural ocean waves are so complicated and variable. To describe the sea surface, the hydrodynamic equations are linearized to obtain a solution of the small amplitude sinusoidal waves.

C.1- Generating Two Dimensional Time-Domain Sea Surface

Synthesizing of the sea surface includes two main procedures, generating the sea surface spectrum, and converting the spectrum into the time domain. The sea spectrum is generated assuming deep waters (waves are not affected by the seabed), a given intensity, fetch, and direction of wind speed (Pierson-Moskowitz and Elfouhaily spectrum models [50], [62]).

Based on the realistic situation, the sea surface is varying instantaneously. In fact, sea state and time must be involved in the sea surface simulation. To assessment of the spectral components of the sea surface, the deep-water transport equation is given [86]:

$$\frac{\partial}{\partial t}\Psi(\mathrm{k},\theta;x,t) + c_g.\nabla\Psi(\mathrm{k},\theta;x,t) = S_i + S_d + S_{nl} \qquad (C.1)$$

where k is the mechanical wavelength, θ is the traveling wave direction along the distance x, during a time t, c_g is the group velocity, and S_i, S_d, S_{nl} are the wind energy, the dissipation energy, and the dispersive transference energy. The statistical properties of the sea surface have been used to present the roughness spectrum $\Psi(\mathrm{k}, \varphi)$ as the Fourier transform of the autocorrelation function of the sea surface. It includes both the radial spectrum $S(\mathrm{k})$ and the angular spreading function $\Phi(\mathrm{k}, \varphi)$. The angular spreading is approximated using a Fourier series expansion of an even real function [50], [86]:

$$\Psi(\mathrm{k}, \varphi) = \frac{1}{\mathrm{k}} S(\mathrm{k}).\, \Phi(\mathrm{k}, \varphi), \qquad (C.2)$$

$$(\mathrm{k}, \varphi) = \frac{1}{2\pi}\left[1 + \sum_{n=1}^{\infty} a_{2n}\,.\cos(2n\varphi)\right], \qquad (C.3)$$

$$\Phi(k, \varphi) \approx \frac{1}{2\pi}[1 + a_2 \cos(2\varphi)]. \qquad (C.4)$$

The generation of the time domain sea surface is performed by generating an initial two-dimensional random process which are filtered by the directional sea surface spectrum [87]. It means, the random phase filtered by $\Psi(k, \varphi)$, and the propagation each frequency that is computed according to the deep-water dispersion relationship.

Appendix D. Sea Surface Spectrum

Based on the project requirement for generating sea surface, several sea surface spectra (JONSWAP, Pierson-Moskowitz, and Elfouhaily et al.) have investigated and simulated. Actually, both spectra (Pierson-Moskowitz, and Elfouhaily et al.) have used to investigate the EM bias, because these are able to generate non-Gaussian roughness surface, which is a criterion to consider EM bias.

D.1- Pierson-Moskowitz Spectrum

One of the most simple ocean spectrum is proposed by Pierson-Moskowitz that assumed the wind blew over the sea surface steadily for a long time, the generated surface waves are equilibrium [62]. It can produce a fully sea surface that includes short and long waves components. To obtain the theoretical description, the experimental collected date have been applied, its relations is given as [62]:

$$S(f) = \alpha . g^2 (2\pi)^{-4} . f^{-5} . \exp\left(-\frac{5}{4}\left(\frac{f_m}{f}\right)^4\right), \qquad (D.1)$$

where, $\alpha = 8.1 \times 10^{-3}$ is Philips cconstant and f_m is the peak frequency, f is the wave frequency in Hz, and g is gravitational acceleration.

D.2- JONSWAP Spectrum

An experimental project the Joint North Sea Wave Observation Project (JONSWAP), data are used to proposing the sea wave spectrum, which is never developed the sea surface fully [86] . In fact, it is a Pierson-Moskowitz spectrum multiplied by an extra factor, it is given [86]:

$$S_j(\omega) = \frac{\alpha g^2}{\omega^5} \exp\left[-\frac{5}{4}\left(\frac{\omega_p}{\omega}\right)^4\right] \gamma^r, \quad (D.2)$$

$$\gamma = \exp\left[-\frac{\left(\omega - \omega_p\right)^2}{2\sigma^2 \omega_p^2}\right]. \quad (D.3)$$

where, ω is the angular frequency and ω_p is peak of the angular frequency.

D.3- Elfouhaily spectrum

Among several ocean spectrum models, Elfouhaily's spectrum has ability to satisfy the fundamental criteria, diverse fetch condition and provide in situ observations. In addition, the two-dimensional wavenumber model has been validating to all wavenumber and electromagnetic usage. The omnidirectional spectrum proposed using sum of both short and long wave spectra, as given [50]:

$$S(k) = k^{-3}[B_l + B_h], \quad (D.4)$$

$$B_l = \frac{1}{2}\alpha_p \frac{c_p}{c} F_p, \quad (D.5)$$

$$B_h = \frac{1}{2}\alpha_m \frac{c_m}{c} F_m. \quad (D.6)$$

where l, h are stand for low and high frequency wave respectively, and B denotes the curvature spectrum, and α_p is the generalized Philip-Kitiagorodskii constant number for long wave, c, c_p are the wave phase speed and wave phase speed at the spectral peak. Also F_p is the long-wave side effect function. In Eqn. D.6 α_m is the generalized Philip-Kitiagorodskii constant number for short-wave, c, c_m are the short-wave phase speed and minimum phase speed, and F_m is the short-wave side effect function.

In this spectrum, the long-wave components assumed aligned with wind direction, but the short wave assumed perpendicular to the wind direction.

Radar observation demonstrated that short gravity wave lose their directionality though the gravity-capillary wave become more directional. finally, the unified full wavenumber approach is rewritten [50]:

$$\Delta(k) = \tanh(a_0 + a_p \left(\frac{c}{c_p}\right)^{2.5} + a_m \left(\frac{c}{c_m}\right)^{2.5}, \qquad \text{(D.7)}$$

here, a_0 is a constant number, and , a_p, a_m are function of c_p, c_m respectively.

Appendix E. List of publications

E.1- Journal or Letter:

1. Ali Ghavidel, D. Schiavulli, and Adriano Camps,"Numerical Computation of the Electromagnetic Bias in GNSS-R Altimetry," IEEE Journal of (Magazine), under revision, 2015.
2. Domenico Schiavulli, Ali Ghavidel, Adriano Camps, Maurizio Migliaccio,"GNSS-R wind-dependent polarimetric signature over the ocean," IEEE Geoscience and Remote Sensing Letters, Submitted, 2015.
3. Ali Ghavidel, and Adriano Camps,"Rain, Swell, And Currents Impact on the EM Bias in GNSS Reflectometry," IEEE Geoscience and Remote Sensing Letters, submitted, March, 2015.
4. Ali Ghavidel, and Adriano Camps,"Time-Domain Statistics of the Electromagnetic Bias In GNSS-Reflectometry," IEEE Geoscience and Remote Sensing Letter, submitted, March, 2015.

E.2- Conference Paper:

5. Ali Ghavidel, and Adriano Camps,"Rain, Swell, And Currents Impact on the EM Bias in GNSS Reflectometry," IEEE Int. GNSS+R 2015 conference, Germany, accepted, 2015.
6. Ali Ghavidel, and Adriano Camps,"Time-Domain Statistics of EM Bias in GNSS Reflectometry," IEEE Int. GNSS+R 2015 conference, Germany, accepted, 2015.
7. Adriano Camps, Hyuk Park, Ali Ghavidel, John Rius, Ivan Sekulic,"GEROS-ISS a demonstration mission of GNSS remote sensing capibilities to drive geophysical parameters of the Earth

surface: performance evaluation", IEEE in Geoscience and Remote Sensing Symposium (IGARSS), accepted, 2015.

8. Ali Ghavidel, Domenico Schiavulli, and Adriano Camps,"A Numerical Simulator to Evaluate the Electromagnetic Bias in GNSS-R Altimetry," IEEE in Geoscience and Remote Sensing Symposium (IGARSS), pp. 4066–4069, 2014.

9. Domenico Schiavulli, Ali Ghavidel, and Adriano Camps,"a Simulator for GNSS-R Polarimetric Observation Over the Ocean", IEEE in Geoscience and Remote Sensing Symposium (IGARSS), pp. 3802 – 3805, 2014.

References

[1] M. Martin-Neira, "A Passive Reflectometry and Interferometry System (PARIS): application to ocean altimetry," *ESA J*, pp. 331–355, 1993.

[2] L.-L. Fu and A. Cazenave, *Satellite altimetry Satellite Altimetry and Earth Sciences*. Academic Press, 2001.

[3] A. W. G. MacGougan, G. Lachapelle, R. Nayak, "Overview of GNSS signal degradation phenomena," *Present. Int. Symp. Kinematic Syst. Geodosy, Geomatics Navig.*, pp. 87–100, 2001.

[4] J. A. Klobuchar, *Ionospheric Effects on GPS, Global Positioning Systems Theory and Applications, Vol I*. American Institute of Aeronautics and Astronautics, 1996.

[5] F. C. Jackson, "The reflection of impulses from a nonlinear random sea," *J. Geophys. Res. Ocean.*, vol. 84, pp. 4939–4943, 1979.

[6] M. A. Srokosz, "On the joint distribution of surface elevation and slopes for a nonlinear random sea, with an application to radar altimetry," *J. Geophys. Res. Ocean.*, vol. 91 C1, pp. 995–1006, 1986.

[7] D. V. Arnold, W. K. Melville, R. H. Stewart, J. A. Kong, W. C. Keller, and E. Lamarre, "Measurements of electromagnetic bias at Ku and C bands," *J. Geophys. Res.*, vol. 100, pp. 969–980, 1995.

[8] T. Elfouhaily, D. Thompson, D. Vandemark, and B. Chapron, "Weakly nonlinear theory and sea state bias estimations," *Journal of Geophysical Research*, 1999. .

[9] T. Elfouhaily, D. R. Thompson, D. Vandemark, and B. Chapron, "Higher-order hydrodynamic modulation: theory and applications for ocean waves," *Proc. R. Soc. A Math. Phys. Eng. Sci.*, vol. 457, no. 2015, pp. 2585–2608, Nov. 2001.

[10] T. Elfouhaily, D. R. Thompson, B. Chapron, and D. Vandemark, "Improved electromagnetic bias theory," *J. Geophys. Res. Ocean.*, vol. 105, pp. 1299–1310, 2000.

[11] E. J. Walsh, F. C. Jackson, D. E. Hines, C. Piazza, L. G. Hevizi, D. J. Mclaughlin, R. E. Mcintosh, R. N. Swift, J. F. Scott, J. K. Yungel, and E. B. Frederick, "Frequency dependence of electromagnetic bias in radar altimeter sea surface range measurements," *J. Geophys. Res. Ocean.*, vol. 96, no. C11, pp. 20571–20583, 1991.

[12] L. G. Hevizi, E. J. Walsh, R. E. McIntosh, D. Vandemark, D. E. Hines, R. N. Swift, and J. F. Scott, "Electromagnetic bias in sea surface range measurements at frequencies of the TOPEX/POSEIDON satellite," *IEEE Trans. Geosci. Remote Sens.*, vol. 31, pp. 376–388, 1993.

[13] F. W. Millet, K. F. Warnick, and D. V. Arnold, “Electromagnetic bias at off-nadir incidence angles,” *J. Geophys. Res.*, vol. 110, no. C9, pp. 1–13, 2005.

[14] F. W. Millet, K. F. Warnick, J. R. Nagel, and D. V Arnold, “Physical optics-based electromagnetic bias theory with surface height – slope cross-correlation and hydrodynamic modulation,” *IEEE Trans. Geosci. Remote Sens.*, vol. 44, no. 6, pp. 1470–1483, 2006.

[15] G. A. Hajj and C. Zuffada, “Theoretical description of a bistatic system for ocean altimetry using the GPS signal,” *Radio Sci.*, vol. 38, no. 5, Oct. 2003.

[16] D. V. T. Elfouhaily, D. R. Thompson, B. Chapron, “Improved electromagnetic bias theory: Inclusion of hydrodynamic modulations,” *J. Geophys. Res. Ocean.*, vol. 106, pp. 4655–4664, 2001.

[17] C. P. Gommenginger, M. A. Srokosz, J. Wolf, and P. A. E. M. Janssen, “An investigation of altimeter sea state bias theories,” *J. Geophys. Res.*, vol. 108, no. C1, p. 3011, 2003.

[18] G. Brown, “The average impulse response of a rough surface and its applications,” *IEEE Trans. Antennas Propag.*, vol. 25, no. 1, pp. 67–74, Jan. 1977.

[19] E. W. B. Hofman-Wellenhof, H. Lichtenegger, *GNSS-Global Navigation Satellite Systems*. Wien and NewYork: Springer, 2008.

[20] “Beidou.” [Online]. Available: http://en.wikipedia.org/wiki/Beidou_.

[21] “QZSS.” [Online]. Available: http://en.wikipedia.org/wiki/Quasi-Zenith_.

[22] T. ElfouhailyD. R. ThompsonB. ChapronD. Vandemark, “Improved electromagnetic bias theory: Inclusion of hydrodynamic modulations,” *J. Geophys. Res. Ocean.*, vol. 106, pp. 4655–4664, 2001.

[23] “IRNSS.” [Online]. Available: http://en.wikipedia.org/wiki/Indian_.

[24] A. Rius, E. Cardellach, and M. Martín-neira, “Altimetric analysis of the Sea-surface GPS-reflected signals,” *IEEE Trans. Geosci. Remote Sens.*, vol. 48, no. 4, pp. 2119–2127, 2010.

[25] A. Camps, H. Park, E. Valencia I Domenech, D. Pascual, F. Martin, A. Rius, S. Ribo, J. Benito, A. Andres-Beivide, P. Saameno, G. Staton, M. Martin-Neira, S. Daddio, and P. Willemsen, “Optimization and performance analysis of interferometric GNSS-R altimeters: Application to the PARIS IoD mission,” *IEEE J. Sel. Top. Appl. Earth Obs. Remote Sens.*, vol. 7, no. 5, pp. 1436–1451, 2014.

[26] H. L. V. Trees, “Detection, estimation, and modulation theory, Part 3 - Radar-sonar signal processing and Gaussian signals in noise,” 1971.

[27] M. Martin-Neira, S. D'Addio, C. Buck, N. Floury, and R. Prieto-Cerdeira, "The PARIS Ocean altimeter," *IEEE Trans. Geosci. Remote Sens.*, vol. 49, no. 6, pp. 2209–2237, 2011.

[28] A. Camps, H. Park, E. Valencia, and A. Rius, "Preliminary error budget of a GNSS-R spaceborne mission," *Int. Geosci. Remote Sens. Symp.*, pp. 3444–3447, 2011.

[29] V. U. Zavorotny and A. G. Voronovich, "Two-scale model and ocean radar Doppler spectra at moderate- and low-grazing angles," *IEEE Trans. Antennas Propag.*, vol. 46, no. 1, pp. 84–92, 1998.

[30] V. U. Zavorotny and A. G. Voronovich, "Scattering of GPS signals from the ocean with wind remote sensing application," *IEEE Trans. Geosci. Remote Sens.*, vol. 38, no. 2, pp. 951–964, Mar. 2000.

[31] J. C. Curlander and and R. N. McDonough, *Synthetic Aperture Radar*. Wiley Interscience, 1991.

[32] K. Borre, D. M. Akos, N. Bertelsen, P. Rinder, and S. H. Jensen, *A software-defined GPS and Galileo receiver a single-frequency approach*. Birkhäuser, 2007.

[33] A. Komjathy, V. U. Zavorotny, P. Axelrad, G. H. Born, and J. L. Garrison, "GPS signal scattering from sea surface : wind speed retrieval using experimental data and theoretical model," *Remote Sens. Environ.*, vol. 73, no. 00, pp. 162–174, 2000.

[34] J. L. Garrison1 and S. J. K. and M. I. Hill, "Effect of sea roughness on bistatically scattered range coded signals from the Global Positioning System," *Geophys. Res. Lett.*, vol. 25, no. 13, pp. 2257–2260, 1998.

[35] A. Camps, M. Vall-Ilossera, J. Miranda, and N. Duffo, "Emissivity of the sea surface roughened by rain: simulation results," *IEEE 2001 Int. Geosci. Remote Sens. Symp.*, vol. 5, no. C, pp. 7031–7033, 2001.

[36] A. Camps, M. Vall-llossera, J. Miranda, and J. Font, "Sea surface brightness temperature at L-band: impact of surface currents," *IEEE Int. Geosci. Remote Sens. Symp.*, vol. 5, no. 1, pp. 3481–3484, 2004.

[37] A. Camps, J. Font, M. Vall-llossera, I. Corbella, N. Duffo, F. Torres, S. Blanch, A. Aguasca, R. Villarino, C. Gabarró, L. Enrique, J. Miranda, R. Sabia, and M. Talone, "Determination of the sea surface emissivity at L-band and application to SMOS salinity retrieval algorithms: Review of the contributions of the UPC-ICM," *Radio Sci.*, vol. 43, no. 3, pp. 1–16, Jun. 2008.

[38] B. S. Yaplee, A. Shapiro, D. L. Hammond, B. D. Au, and E. A. Uliana, "Nanosecond radar observations of the ocean surface from a stable platform," *IEEE Trans. Geosci. Electron.*, vol. 9, no. 3, 1971.

[39] M. S. Longuet-Higgins, "The effect of non-linearities on statistical distributions in the theory of sea waves," *J. Fluid Mech.*, vol. 17, no. 1955, pp. 459–480, 1963.

[40] C. D. Hall and R. A. Cordey, “Multistatic scatterometry,” *IEEE nternational Geosci. Remote Sens. Symp. Remote Sens. Symp.*, vol. 1, pp. 561–562, 1988.

[41] D. E. Barrick and W. H. Peake, “A review of scattering from surfaces with different roughness scales,” *Radio Sci.*, vol. 3, pp. 865– 868, 1968.

[42] M. S. Longuet-Higgins, “The statistical geometry of random surfaces,” *Proc. Symp. Appl. Math. Hydrodyn. Instab. Amer. Math. Soc*, pp. 105–143, 1962.

[43] R. E. Glazman, A. Fabrikant, and M. A. Srokosz, “Numerical analysis of the sea state bias for satellite altimetry,” *J. Geophys. Res. Ocean.*, vol. 101, pp. 3789–3799, 1996.

[44] W. Alpers and K. Hasselmann, “The two-frequency microwave technique for measuring ocean-wave spectra from an airplane or satellite,” *Boundary-Layer Meteorol.*, vol. 13, pp. 215–230, 1978.

[45] E. Rodríguez, Y. KimJan, and M. Martin, “The effect of small-wave modulation on the electromagnetic bias,” *J. Geophys. Res. Ocean.*, vol. 98, pp. 2379–2389, 1992.

[46] R. T. S. L. Tsang, J. A. Kong, *Theory of Microwave Remote Sensing*. New York: Wiley-Interscience, 1985.

[47] G. L. Tyler, “Wavelength dependence in radio-wave scattering and specular-point theory,” *Radio Sci.*, vol. 11, no. 2, pp. 83–91, 1976.

[48] D. E. Barrick and B. J. Lipa, “Analysis and interpretation of altimeter sea echo,” *Adv. Geophys.*, vol. 27, pp. 61–100, 1960.

[49] T. Elfouhaily, D. R. Thompson, and L. Linstrom, “Delay-Doppler analysis of bistatically reflected signals from the ocean surface: theory and application,” *IEEE Trans. Geosci. Remote Sens.*, vol. 40, no. 3, pp. 560–573, Mar. 2002.

[50] T. Elfouhaily, B. Chapron, K. Katsaros, and D. Vandemark, “A unified directional spectrum for long and short wind-driven waves,” *J. Geophys. Res.*, vol. 102, no. C7, p. 15781, 1997.

[51] A. Ghavidel, D. Schiavulli, and A. Camps, “A numerical simulator to evaluate the electromagnetic bias in GNSS-R altimetry,” in *IEEE Int. Geoscience and Remote Sensing Symposium*, 2014, pp. 4066–4069.

[52] A. Ghavidel, D. Schiavulli, and A. Camps, “Numerical computation of the electromagnetic bias in GNSS-R altimetry,” *JSTAR*, p. submiting, 2015.

[53] G. Picardi, R. Seu, S. G. Sorge, and M. M. Neira, “Bistatic model of ocean scattering,” *IEEE Trans. Antennas Propag.*, vol. 46, no. 10, pp. 1531–1541, 1998.

[54] D. B. Creamer, F. Henyey, R. Schult, and J. Wright, “Improved linear representation of ocean surface waves,” *J. Fluid Mech.*, vol. 205, no. 1, pp. 135–161, Apr. 1989.

[55] P. Naenna and J. T. Johnson, “A Monte Carlo study of altimeter pulse returns and the electromagnetic bias,” *IEEE Trans. Geosci. Remote Sens.*, vol. 48, no. 8, pp. 3218–3224, 2010.

[56] L. A. Pierson, Willard J., Jr. and Moskowitz, “Proposed Spectral Form for Fully Developed Wind Seas Based on the Similarity Theory of S. A. Kitaigorodskii.”

[57] M. S. Longuet-Higgins, “Observation of the directional spectrum of sea waves using the motions of a flotation buoy,” *Ocean Wave spectra*, pp. 111–136, 1963.

[58] V. I. Tatarskii and V. V. Tatarskii, “Statistical non-Gaussian model of sea surface with anisotropic spectrum for wave scattering theory. Part I,” *Prog. Electromagn. Res.*, vol. PIER 22, pp. 259–291, 1999.

[59] C. A. Balanis, *Advanced engineering electromagnetics*. John Wiley & Sons, 1989.

[60] M. P. Clarizia, C. Gommenginger, M. D. Bisceglie, C. Galdi, and M. A. Srokosz, “Simulation of L-Band Bistatic Returns From the Ocean Surface: A Facet Approach With Application to Ocean GNSS Reflectometry,” *IEEE Transactions on Geoscience and Remote Sensing*, vol. 50, no. 3, pp. 960–971, 2011.

[61] K. F. Warnick and D. V. Arnold, “Generalization of the Geometrical Optics Scattering Limit for a Rough Conducting Surface,” *IGARSS ’98. Sens. Manag. Environ.*, vol. 3, pp. 1472–1474, 1998.

[62] W. J. Pierson and L. Moskowitz, “A proposed spectral form for fully developed wind seas based on the similarity theory of S. A. Kitaigorodskii,” *J. Geophys. Res.*, vol. 69, pp. 5181–5190, 1964.

[63] J. T. Johnson, J. V. Toporkov, and G. S. Brown, “A numerical study of backscattering from time-evolving sea surfaces: comparison of hydrodynamic models,” *IEEE Transactions on Geoscience and Remote Sensing*, vol. 39, no. 11, pp. 2411–2420, 2001.

[64] N. I. Nickolaev, O. I. Yordanov, and M. A. Mickalev, “Radar backscattering from non-Gaussian sea surface,” *Proc. IGARSS’Remote Sens. Glob. Monit. Earth Manag. Sens. Glob. Monit. Earth Manag.*, vol. 3, pp. 1275–1278, 1991.

[65] N. I. Nickolaev, O. I. Yordanov, and M. A. Michalev, “Non-Gaussian effects in the two-scale model for rough surface scattering,” *J. Geophys. Res.*, vol. 97, no. C10, pp. 15617–15624, 1992.

[66] V. V. Tatarskii and V. I. Tatarskii, “Non-Gaussian statistical model of the ocean surface for wave-scattering theories,” *Waves in Random Media*, vol. 6, pp. 419–435, 1996.

[67] V. I. Tatarskii and G. A. Voronovich, “The role of non-Gaussian probability distribution in the wave scattering by rough surface theory,” *Proc. PIERS*, vol. 94354, 1994.

[68] C. Cox and W. Munk, “Measurement of the roughness of the sea surface from photographs of the sun’s glitter,” *J. Opt. Soc. Am.*, vol. 11, pp. 838–850, 1954.

[69] C. Cox and W. Munk, “Statistics of the sea surface derived from sun glitter,” *J. Mar. Res.*, vol. 13, pp. 198–227, 1954.

[70] N. Huang and S. r. Long, “An experimental study of the surface elevation probability distribution and statistics of wind-generated waves,” *J. fluid Mech*, vol. 101, pp. 179–220, 1980.

[71] J. M. Rius, M. Ferrando, and L. Jofre, “GRECO: graphical electromagnetic computing for RCS prediction in real time,” *IEEE Antennas Propag. Mag.*, vol. 35, no. 2, pp. 7–17, Apr. 1993.

[72] D. J. Donohue, H. Ku, D. R. Thompson, and J. Sadowsky, “Direct numerical simulation of electromagnetic rough surface and sea scattering by an improved banded matrix iterative method,” *Johns Hopkins APL Tech. Dig. (Applied Phys. Lab.*, vol. 18, no. 2, pp. 204–215, 1997.

[73] L. F. Bliven, P. W. Sobieski, and C. Craeye, “Rain generated ring-wave: measurements and modeling for remote sensgin,” *Int. J. Remote Sens.*, vol. 18, no. 1, pp. 221–228, 1997.

[74] C. Craeye, P. W. Sobieski, and L. F. Bliven, “Scattering by artificial wind and rain roughened water surfaces at oblique incidences,” *Int. J. Remote Sens.*, vol. 18, no. 10, pp. 2241–2246, 1997.

[75] S. Durden and J. Vesecky, “A physical radar cross-section model for a wind-driven sea with swell,” *IEEE J. Ocean. Eng.*, vol. 10, no. 4, pp. 445–451, 1985.

[76] N. E. Huang, D. T. Chen, C.-C. Tung, and J. R. Smith, “Interactions between Steady Won-Uniform Currents and Gravity Waves with Applications for Current Measurements,” *J. Phys. Oceanogr.*, vol. 2, no. 4, pp. 420–431, 1972.

[77] J. Miranda, M. Vall-Ilossera, R. Villarino, and A. Camps, “Sea state and rain effects on sea surface emissivity at L-band,” *Eur. Sp. Agency*, no. 525, pp. 155–163, 2003.

[78] M. J. Manton, “On the attenuation of sea waves by rain,” *Geophys. Fluid Dyn.*, vol. 5, no. 1, pp. 249–260, 1973.

[79] J. W. Wright, “A new model for sea clutter,” *Antennas Propagation, IEEE Trans.*, vol. 16, pp. 217–223, 1968.

[80] F. Bass, I. Fuks, A. Kalmykov, I. Ostrovsky, and A. Rosenberg, “Very high frequency radiowave scattering by a disturbed sea surface Part I: Scattering from a slightly disturbed boundary,” *IEEE Trans. Antennas Propag.*, vol. 16, 1968.

[81] J. Park, J. T. Johnson, and S. T. Lowe, “A study of the electromagnetic bias in GNSS-R altimetry,” *Int. Geosci. Remote Sens. Symp. Quebec, Canada*, pp. 2–4, 2014.

[82] Oak Road Systems, “Measures of Shape: Skewness and Kurtosis,” *http://www.tc3.edu/instruct/sbrown/stat/shape.htm*, 2012. .

[83] F. T. Ulaby, R. K. Moore, and Adrian K. Fung, *Microwave remote sensing: active and passive, Volume II: radar remote sensing and surface scattering and emission theory*. Artech House, 1986.

[84] A. J. Gasiewski and D. B. Kunkee, “Polarized microwave emission from water waves,” *Radio Sci.*, vol. 29, no. 6, pp. 1449–1466, 1994.

[85] F. T. Ulaby, R. K. Moore, and A. K. Fung, *Microwave remote sensing: Active and passive, Volume 1 - Microwave remote sensing fundamentals and radiometry*. 1981.

[86] K. Hasselmann, “On the non-linear energy transfer in a gravity-wave spectrum Part 1. General theory,” *J. Fluid Mech.*, vol. 12, no. 4, pp. 481–500, 1962.

[87] G. Mastin, P. Watterberg, and J. Mareda, “Fourier synthesis of ocean scenes,” *IEEE Comput. Graph. Appl.*, vol. 7, no. 3, pp. 16–23, Mar. 1987.